JACS
JOURNAL OF THE AMERICAN CHEMICAL SOCIETY

Article

pubs.acs.org/JACS

Optimizing Millisecond Time Scale Near-Infrared Emission in Polynuclear Chrome(III)−Lanthanide(III) Complexes

Lilit Aboshyan-Sorgho,[†] Homayoun Nozary,[†] Annina Aebischer,[§] Jean-Claude G. Bünzli,*[,§] Pierre-Yves Morgantini,[‡] Kevin R. Kittilstved,[‡] Andreas Hauser,*[,‡] Svetlana V. Eliseeva,[∥,⊥] Stéphane Petoud,*[,∥,#] and Claude Piguet*[,†]

[†]Department of Inorganic, Analytical and Applied Chemistry, and [‡]Department of Physical Chemistry, University of Geneva, 30 quai Ernest-Ansermet, CH-1211 Geneva 4, Switzerland

[§]Institute of Chemical Sciences and Engineering, Ecole Polytechnique Fédérale de Lausanne, CH-1015 Lausanne, Switzerland, and Center for Next Generation Photovoltaic Systems, Korea University, Sejong Campus, Jochiwon, Chungnam 339700, South Korea

[∥]Centre de Biophysique Moléculaire, CNRS UPR 4301, Rue Charles Sadron, 45071 Orléans Cedex 2, France

[⊥]Le Studium, Institute for Advanced Studies, Orléans and Tours, France

[#]Department of Chemistry, University of Pittsburgh, 219 Parkman Avenue, Pittsburgh, Pennsylvania 15260, United States

Supporting Information

ABSTRACT: This work illustrates a simple approach for optimizing long-lived near-infrared lanthanide-centered luminescence using trivalent chromium chromophores as sensitizers. Reactions of the segmental ligand **L2** with stoichiometric amounts of $M(CF_3SO_3)_2$ (M = Cr, Zn) and $Ln(CF_3SO_3)_3$ (Ln = Nd, Er, Yb) under aerobic conditions quantitatively yield the D_3-symmetrical trinuclear $[MLnM(\mathbf{L2})_3](CF_3SO_3)_n$ complexes (M = Zn, n = 7; M = Cr, n = 9), in which the central lanthanide activator is sandwiched between the two transition metal cations. Visible or NIR irradiation of the peripheral Cr(III) chromophores in $[CrLnCr(\mathbf{L2})_3]^{9+}$ induces rate-limiting intramolecular intermetallic Cr→Ln energy transfer processes (Ln = Nd, Er, Yb), which eventually produces lanthanide-centered near-infrared (NIR) or IR emission with apparent lifetimes within the millisecond range. As compared to the parent dinuclear complexes $[CrLn(\mathbf{L1})_3]^{6+}$, the connection of a second strong-field $[CrN_6]$ sensitizer in $[CrLnCr(\mathbf{L2})_3]^{9+}$ significantly enhances the emission intensity without perturbing the kinetic regime. This work opens novel exciting photophysical perspectives via the buildup of non-negligible population densities for the long-lived doubly excited state $[Cr^*LnCr^*(\mathbf{L2})_3]^{9+}$ under reasonable pumping powers.

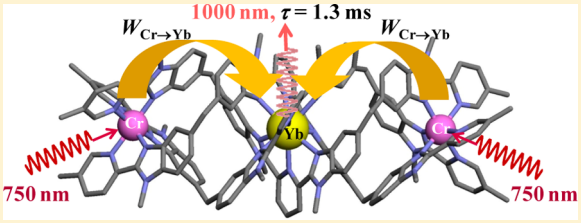

INTRODUCTION

Formally, the near-infrared (NIR) spectral range starts at 750 nm (13 333 cm^{-1}), and many trivalent lanthanide ions, Ln(III) = Pr, Nd, Sm, Dy, Ho, Er, Tm, and Yb, display radiative f−f transitions above this wavelength.[1] Those with Ln = Nd, Er, and Yb are often exploited for applications as optical amplifiers (for instance, in Er-doped silica fibers, which are transparent around 1550 nm, the wavelength of the Er($^4I_{13/2}$→$^4I_{15/2}$) emission),[2] as laser materials (for instance, in Nd:YAG lasers based on the Nd($^4F_{3/2}$→$^4I_{11/2}$) transition at 1060−1090 nm),[3] as NIR→visible light upconverting devices,[4] and as luminescent probes for high-resolution analysis of deep living tissues (light transmission is maximized in the 850−1100 nm spectral range for biological material).[5] In this context, hundreds of lanthanide-containing NIR emitters were synthesized and investigated during the past decade,[6] with a special emphasis on the connection of sophisticated organic chromophores that are able to harvest near-UV or visible light for sensitizing NIR emission.[7] Because energy transfer processes are optimized when the spectral overlap integral between the emission spectrum of the donor (i.e., that of the light-harvesting chromophore) and the absorption spectrum of the lanthanide activator is maximized,[6] highly conjugated polyaromatic antennae emitting in the red part of the electromagnetic spectrum[7] are actively investigated for improving the global sensitization process.[8] However, the focus of many studies on practical applications has somewhat masked some of the less-common photophysical properties of molecular lanthanide-centered NIR emissive complexes, which are currently underexploited. First, the estimated effective vibrational energies $\hbar\omega_{eff} \approx 2000$ cm^{-1} operative in molecular coordination complexes,[9] combined with interactions of the metallic centers with solvent molecules possessing high-energy CH, OH, and NH oscillators, are particularly efficient for inducing nonradiative deexcitation pathways in lanthanide-centered NIR emitters. Consequently, the characteristic luminescence lifetimes of NIR-emitting Ln(III) ions, $\tau_{Ln} = 1/k_{Ln}$, are on the (sub)microsecond time scale, which is far below their predicted millisecond radiative decays.[6,7] Because biological materials

Received: April 26, 2012
Published: June 22, 2012

   dx.doi.org/10.1021/ja304009b | J. Am. Chem. Soc. 2012, 134, 12675−12684

irradiated in the visible do not produce strong background emission in the NIR range, time-gated amplification is not considered an important issue for short-term applications, and only few efforts have been focused on the lengthening of NIR lanthanide lifetimes in molecular systems.[10] However, millisecond NIR lifetimes should offer remarkable opportunities (i) for security and identification systems that cannot be forged and (ii) for the quantification of trace targets in biological materials with time-gated detection. Second, broadband light-harvesting organic chromophores can be favorably replaced with d-block sensitizers possessing much narrower and tunable absorption bands to facilitate the design of more specific excitation/emission wavelength pairs.[11]

Pseudo-octahedral trivalent chromium chromophores are particularly attractive as sensitizers in this context[12] because two broad and spin-allowed transitions ($^4T_1$, $^4T_2 \leftarrow {}^4A_2$) are available in the UV−visible domain, while narrow spin-forbidden excited states are accessible in the visible ($^2T_2 \leftarrow {}^4A_2$) and in the NIR region ($^2T_1$, $^2E \leftarrow {}^4A_2$, Figure S1, Supporting Information).[13] For instance, cocrystallization of $[Cr(CN)_6]^{3-}$[14] with Nd(III) and Yb(III) cations gives infinite $[Cr(CN)_4(\mu\text{-}CN)_2Ln(H_2O)_2(dmf)_4]_\infty$ chains, in which the NIR emitting lanthanides could be indirectly sensitized by the blue excitation of the spin-allowed $Cr(^4T_2 \leftarrow {}^4A_2)$ transition.[15] However, the efficient intermetallic Cr→Ln energy transfer processes operating in these coordination polymers ($W_{Cr\rightarrow Ln} > 10^8\ s^{-1}$) did not offer a possibility for lengthening the Ln(III)-centered emission lifetimes.[16]

To restrain Cr/Ln communication to an isolated pair of metals, for which the intermetallic energy transfer rate constant can be controlled, Kaizaki[17] and Piguet[18] designed two families of dinuclear Cr(III)/Ln(III) molecular complexes exhibiting Ln-centered NIR emission upon Cr(III) sensitization (Figure 1). The detection of residual $Cr(^2E \rightarrow {}^4A_2)$ emission together with the target $Yb(^2F_{5/2} \rightarrow {}^2F_{7/2})$ fluorescence upon visible or NIR irradiation (Figure 1) confirmed that incomplete intramolecular Cr→Yb energy transfers occur due to small $W_{Cr\rightarrow Yb}$ rate constants, thus leading to long apparent Yb-centered NIR lifetimes mirroring the millisecond decay of the Cr(III) donor chromophore,[10,16] but to small quantum yields. In this Article, we propose a simple and efficient strategy for optimizing lanthanide-centered emission intensity in such edifices by increasing their nuclearity and apply it to Ln = Nd, Er, and Yb.

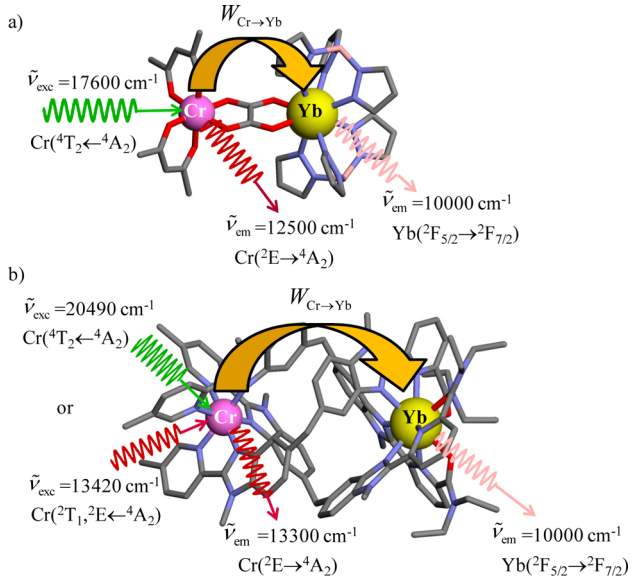

Figure 1. Cr(III)-sensitized Yb-centered NIR emission occurring in isolated dinuclear complexes (a) $[(acac)_2Cr(ox)Yb(HB(pz)_3)_2]$ (Cr···Yb = 5.67 Å)[17] and (b) $[CrYb(\mathbf{L1})_3]^{6+}$ (Cr···Yb = 9.33 Å).[18]

RESULTS AND DISCUSSION

Theoretical Background. The complete light-conversion processes in the dinuclear CrLn helicates can be modeled with the Jablonski diagram depicted in Figure 2a for Ln = Yb.[19] The solutions of the associated kinetic differential equations, given in matrix form in eq 1,[20] under continuous-wave irradiation of the Cr-centered transitions yield the variations of the steady-state population densities $N^{|i\rangle}$ versus increasing pump power shown in Figure 2b. In eq 1, $W_{Cr\rightarrow Yb}$ is the energy transfer rate constant measured in $[CrYb(\mathbf{L1})_3]^{6+}$, k_{Cr}^{CrGd} is the decay rate constant of $Cr(^2E)$ in the absence of an acceptor and measured in $[CrGd(\mathbf{L1})_3]^{6+}$, while k_{Yb}^{ZnYb} is the decay rate constant of $Yb(^2F_{5/2})$ in the absence of a donor and measured in $[ZnYb(\mathbf{L1})_3]^{5+}$. The pumping rate constant, k_{Cr}^{exc}, is given by eq 2[21] in which σ_{Cr} is the absorption cross section of the Cr-centered transition[22] and λ_p is the pump wavelength, ω_p is the pump radius, P is the incident pump power, h is the Planck constant, and c is the vacuum speed of light.

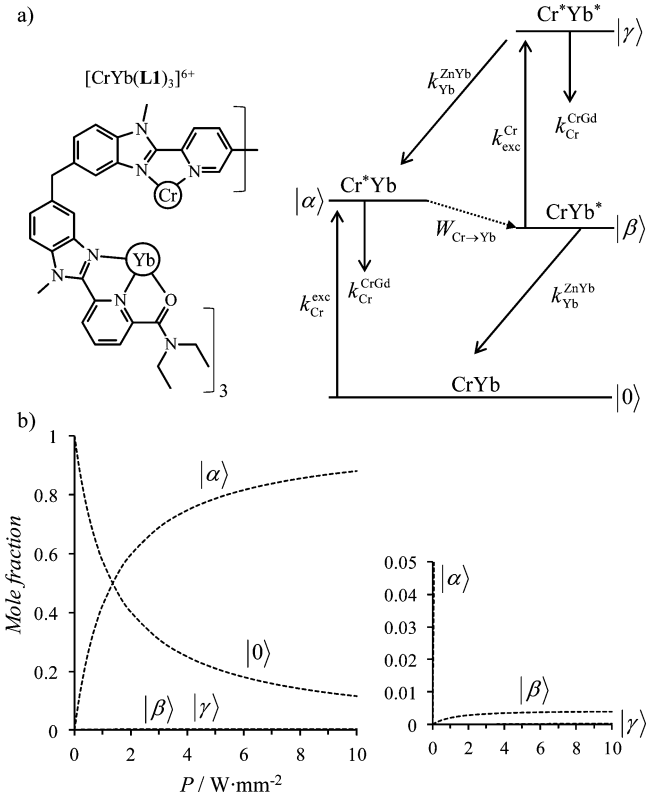

Figure 2. (a) Kinetic scheme for modeling the light-conversion process operating in $[CrYb(\mathbf{L1})_3]^{6+}$ upon irradiation into the Cr-centered absorption bands[19] and (b) computed steady-state population densities for the various levels (the 0−0.05 population density range is highlighted on the right) by using $W_{Cr\rightarrow Yb} = 240\ s^{-1}$, $k_{Cr}^{CrGd} = 270\ s^{-1}$, and $k_{Yb}^{ZnYb} = 5 \times 10^4\ s^{-1}$ with increasing incident pump power P (Cr = $Cr(^4A_2)$ ground state, Yb = $Yb(^2F_{7/2})$ ground state, Cr* = $Cr(^2E)$ excited state, and Yb* = $Yb(^2F_{5/2})$ excited state).[16]

dx.doi.org/10.1021/ja304009b | J. Am. Chem. Soc. 2012, 134, 12675−12684

$$\left[\frac{dN^{|i\rangle}}{dt}\right] = \boldsymbol{M} \times \left[N^{|i\rangle}\right] \text{ with } \boldsymbol{M} =$$

$$\begin{pmatrix} -k_{Cr}^{exc} & k_{Cr}^{CrGd} & k_{Yb}^{ZnYb} & 0 \\ k_{Cr}^{exc} & -\left(k_{Cr}^{CrGd} + W_{Cr\rightarrow Yb}\right) & 0 & k_{Yb}^{ZnYb} \\ 0 & W_{Cr\rightarrow Yb} & -\left(k_{Yb}^{ZnYb} + k_{Cr}^{exc}\right) & k_{Cr}^{CrGd} \\ 0 & 0 & k_{Cr}^{exc} & -\left(k_{Cr}^{CrGd} + k_{Yb}^{ZnYb}\right) \end{pmatrix} \quad (1)$$

$$k_{Cr}^{exc} = \frac{\lambda_P}{hc\pi(\omega_P)^2} P\sigma_{Cr} = fP\sigma_{Cr} \quad (2)$$

Because $(k_{Cr}^{CrGd} + W_{Cr\rightarrow Yb}) \ll k_{Yb}^{ZnYb}$, the population densities of the Yb-centered excited levels $|\beta\rangle$ and $|\gamma\rangle$ remain negligible for all incident pump powers, and as the intrinsic luminescence quantum efficiency of the Yb luminescence, η_{Yb}^{Yb}, is low, the intensity of the NIR emission remains marginal ($I \propto \eta_{Yb}^{Yb}(N^{|\beta\rangle} + N^{|\gamma\rangle})$, Figure S2, Supporting Information). However, its apparent exponential decay $\tau_{Yb}^{CrYb} = 1/k_{Yb}^{CrYb} = 1.96$ ms in $[CrYb(\mathbf{L1})_3]^{6+}$ mirrors the long $Cr(^2E)$ donor lifetime.[16]

With this in mind, the only available option for improving emission intensity in molecular edifices without affecting the apparent millisecond dynamics of the Yb-centered NIR emission observed in dinuclear helicates requires the connection of additional Cr(III) sensitizers with identical photophysical properties. A first step toward this goal is to extend the polynuclear axis by addition of a second terminal Cr(III) ion. The trinuclear dimetallic complex $[CrYbCr(\mathbf{L2})_3]^{9+}$ is expected to meet the above-mentioned criterion (Figure 3a):[23] introduction of the rate constants obtained for $[CrYb(\mathbf{L1})_3]^{6+}$ into a kinetic scheme adapted to $[CrYbCr(\mathbf{L2})_3]^{9+}$ (Figure 3b, $k_{Cr}^{CrGdCr} \equiv k_{Cr}^{CrGd}$, $k_{Yb}^{ZnYbZn} \equiv k_{Yb}^{ZnYb}$, and $W_{Cr\rightarrow Yb}^{CrYbCr} \equiv W_{Cr\rightarrow Yb}^{CrYb} = W_{Cr\rightarrow Yb}$) logically predicts a statistical increase of the intensity of the NIR emission by a factor: $f_{gain} = 2$ (Figure S2, Supporting Information). It is worth noting here that the Yb-centered NIR luminescence in $[CrYbCr(\mathbf{L2})_3]^{9+}$ is expected to mainly originate from the singly excited state CrYb*Cr ($|\beta\rangle$ in Figure 3b) at low incident pump power, as found for $[CrYb(\mathbf{L1})_3]^{6+}$, whereas the doubly excited state Cr*Yb*Cr ($|\gamma\rangle$ in Figure 3b) becomes the main contributor at higher incident pump power (Figure S3b, Supporting Information), a characteristic inherent to the trinuclear molecular complex.

In the following sections, the accuracy of these predictions for the complete molecular light-conversion process leading to NIR emission in the trinuclear complexes is demonstrated for $[CrLnCr(\mathbf{L2})_3]^{9+}$ (Ln = Nd, Er, Yb) in which the twin d-block metal ions act as sensitizers, as well as for the reference helicates $[ZnLnZn(\mathbf{L2})_3]^{7+}$ for which no d-block sensitization is present.

Synthesis and Structural Characterization of $[ZnLnZn(\mathbf{L2})_3](CF_3SO_3)_7$ and $[CrLnCr(\mathbf{L2})_3](CF_3SO_3)_9$ (Ln = Nd, Er, Yb). Stoichiometric mixing of $M(CF_3SO_3)_2{\cdot}xH_2O$ (M = Cr(II), Zn(II); 2 equiv) and $Ln(CF_3SO_3)_3{\cdot}nH_2O$ (Ln = Nd, Er, Yb; 1 equiv) with the segmental tridentate ligand **L2** (3 equiv) in acetonitrile quantitatively yields the targeted self-assembled triple-stranded complexes $[MLnM(\mathbf{L2})_3]^{7+}$ as previously established for Ln = La, Eu, Gd, Tb, and Lu (Figure 3a).[23a] Whereas the air-sensitive dinuclear chromium(II) complexes are not isolated, slow diffusion of diethyl ether into concentrated acetonitrile solutions of the zinc(II) complexes gives 75−80% yield of $[ZnLnZn(\mathbf{L2})_3](CF_3SO_3)_7{\cdot}nH_2O$ (Table S1) whose ESI-MS (Table S2 and Figure S4a) and

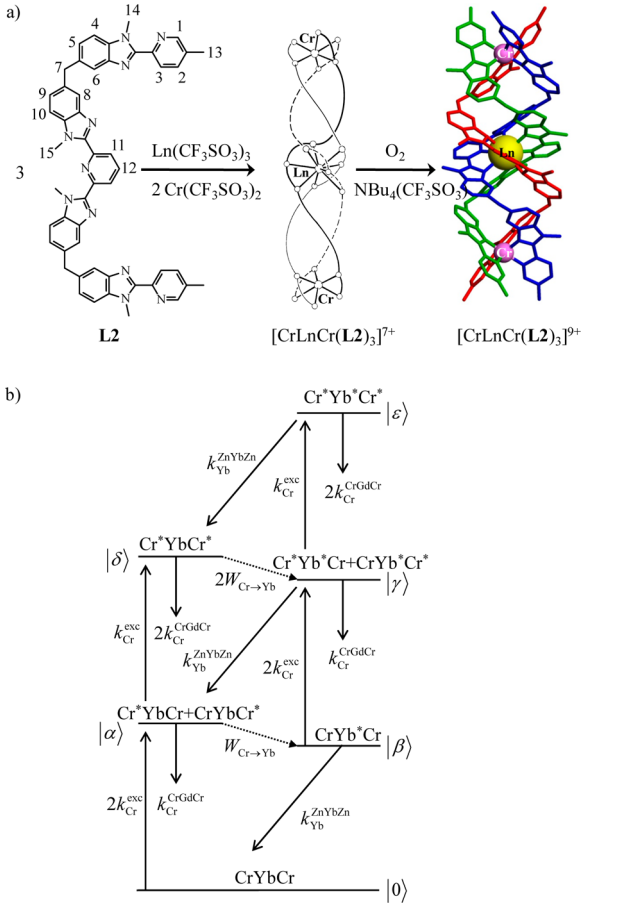

Figure 3. (a) Self-assembly of the trinuclear complexes $[CrLnCr(\mathbf{L2})_3]^{9+}$[23] and (b) adapted kinetic scheme for modeling the light-conversion process operating in $[CrYbCr(\mathbf{L2})_3]^{9+}$ upon irradiation of the Cr-centered transitions (Cr = $Cr(^4A_2)$ ground state, Yb = $Yb(^2F_{7/2})$ ground state, Cr* = $Cr(^2E)$ excited state, and Yb* = $Yb(^2F_{5/2})$ excited state).[18b]

paramagnetically shifted ^1H NMR spectra (Ln = Nd, Yb, Table S3 and Figure S5) are diagnostic for the systematic formation of D_3-symmetrical triple-stranded helicates $[ZnLnZn(\mathbf{L2})_3]^{7+}$.[23] Despite several attempts, we were unable to obtain X-ray quality crystals for these complexes. Therefore, a DFT-optimized gas-phase molecular structure was computed for $[ZnEuZn(\mathbf{L2})_3]^{7+}$ (Figure 4a). For M = Cr, the intermediate $[CrLnCr(\mathbf{L2})_3]^{7+}$ complexes undergo fast air oxidation to give $[CrLnCr(\mathbf{L2})_3](CF_3SO_3)_9{\cdot}m$TBAf$\cdot nH_2O$ after slow diffusion of diethyl ether into concentrated acetonitrile solutions containing an excess of $Bu_4N(CF_3SO_3)$ (=TBAf, Table S1). Because of the slow electronic relaxation rate of the nondegenerate $Cr(^4A_2)$ ground state,[24] ^1H NMR spectra are too broad for any reliable characterization of these complexes (Figure S6), but ESI-MS data strongly support the exclusive formation of $[CrLnCr(\mathbf{L2})_3]^{9+}$ in acetonitrile (Table S2 and Figure S4b). Recrystallization by slow diffusion of diethylether into propionitrile solutions yields fragile orange needles of $[CrLnCr(\mathbf{L2})_3](CF_3SO_3)_9(C_3H_5N)_{30}$ (Ln = Eu, Gd, Tb, Er, Yb, Lu) suitable for X-ray diffraction studies. All complexes are isostructural (monoclinic, $P2_1/c$) with huge unit cells ($V \approx 48\,000$ Å^3, $Z = 4$) and limited diffraction intensities, which require synchrotron facilities for collecting suitable sets of diffraction data. Ln = Eu (midrange sized lanthanide) and Ln = Yb (small sized lanthanide) have been selected for further structural

dx.doi.org/10.1021/ja304009b | J. Am. Chem. Soc. 2012, 134, 12675−12684

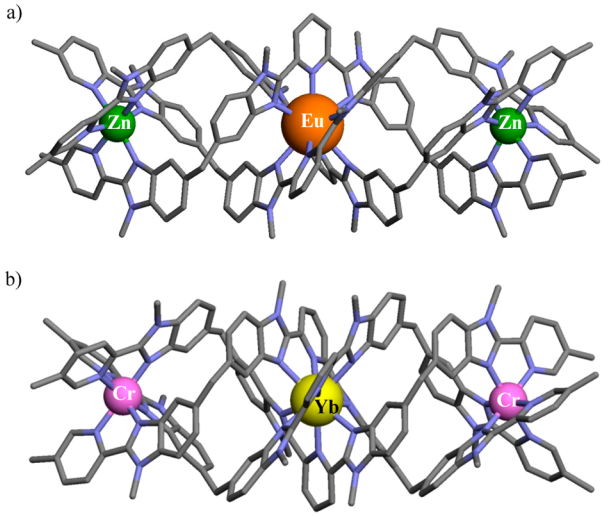

Figure 4. Color-coded perspective views of (a) the DFT-optimized gas-phase structure of $[ZnEuZn(\mathbf{L2})_3]^{7+}$ and (b) the molecular structure of $[CrYbCr(\mathbf{L2})_3]^{9+}$ in the crystal structure of $[CrYbCr(\mathbf{L2})_3](CF_3SO_3)_9(C_3H_5N)_{30}$. Hydrogen atoms have been omitted for clarity (C = gray, N = blue).

analyses, and their crystal structures indeed confirm the existence of almost superimposable pseudo-D_3 symmetrical triple-stranded helical cations (Figures S7–S9), together with disordered noncoordinated triflate anions and propionitrile molecules (Figure 4b).[25] DFT-optimized Zn–N and Eu–N bond lengths in $[ZnEuZn(\mathbf{L2})_3]^{7+}$, and observed Cr–N and Ln–N bond lengths in $[CrLnCr(\mathbf{L2})_3]^{9+}$, have standard values.[18,26] The d-block atoms (Zn or Cr) occupy axially compressed pseudo-octahedral sites produced by the three bound terminal chelating didentate benzimidazole-pyridine units, while trivalent lanthanides lie in the central pseudo-tricapped trigonal prismatic cavities provided by the nine heterocyclic nitrogen atoms of the three wrapped tridentate segments. The average intramolecular intermetallic Zn···Ln distance of 9.74 Å estimated for $[ZnEuZn(\mathbf{L2})_3]^{7+}$ in the gas phase is marginally longer than related Cr···Ln separations measured in $[CrLnCr(\mathbf{L2})_3]^{9+}$ (8.59–9.02 Å; average 8.86 Å).[23b] These values compare well with 8.96 and 9.33 Å distances previously reported for the parent dinuclear $[ZnEu(\mathbf{L1})_3]^{5+}$[26] and $[CrLn(\mathbf{L1})_3]^{6+}$[18] complexes in the solid state.

Beyond the helical twist, which is increased by a half turn on going from $[CrLn(\mathbf{L1})_3]^{6+}$ (0.78 turn for a total linear progression of 12.01 Å, pitch = 15.4 Å)[18] to $[CrLnCr(\mathbf{L2})_3]^{9+}$ (1.30 turns for a total linear progression of 19.78 Å, pitch = 15.2 Å), the connection of the second Cr(III) sensitizer in $[CrLnCr(\mathbf{L2})_3]^{9+}$ further affects the lanthanide coordination sphere because the terminal pseudo-C_3 nine-coordinated LnN_6O_3 metallic unit in $[CrLn(\mathbf{L1})_3]^{6+}$ (Figure 1b) is transformed into a central pseudo-D_3 LnN_9 entity in $[CrLnCr(\mathbf{L2})_3]^{9+}$ (Figure 4b).

Photophysical Properties of Isolated Ligand-Centered and Metal-Centered Chromophores in $[ZnLnZn(L2)_3](CF_3SO_3)_7$ (Ln = Gd, Nd, Er, Yb) and $[CrGdCr(L2)_3](CF_3SO_3)_9$. The free polyaromatic ligand **L2** strongly absorbs UV irradiation via a series of allowed $\pi\rightarrow\pi^*$ transitions whose apparent maximum band envelope lies at 31 500 cm^{-1} (Table S4, Supporting Information). UV-photoexcitation into these bands produces a structured blue-green fluorescence arising from the lowest singlet state ($^1\pi^*\rightarrow\pi$; 22 780 cm^{-1}), but no phosphorescence was detectable.[23a] Upon coordination to optically inactive metallic cations in the trinuclear complex $[ZnGdZn(\mathbf{L2})_3]^{7+}$,[27] standard excitonic coupling between the three bound wrapped aromatic binding units splits the $\pi\rightarrow\pi^*$ transitions into two principal components (30 675 and 26 180 cm^{-1}).[28] This gives an opportunity for extending ligand-centered excitation from UV to visible, and irradiation of $[ZnGdZn(\mathbf{L2})_3]^{7+}$ in the 30 770–24 690 cm^{-1} domain indeed produces fluorescence ($^1\pi^*\rightarrow\pi$ at 22 520 cm^{-1}) and phosphorescence ($^3\pi^*\rightarrow\pi$ at 20 100 cm^{-1}, τ = 2.45(9) ms, Figure 5).[23a]

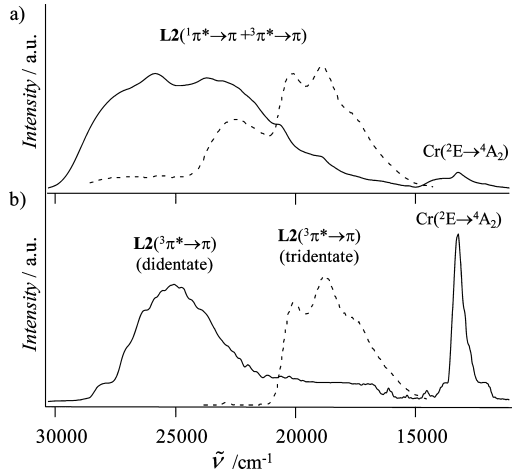

Figure 5. (a) Fluorescence and (b) phosphorescence (delay time after flash = 0.05 ms) spectra recorded for $[ZnGdZn(\mathbf{L2})_3](CF_3SO_3)_7$ (dashed line, $\tilde{\nu}_{exc}$ = 30 770 cm^{-1}) and $[CrGdCr(\mathbf{L2})_3](CF_3SO_3)_9$ (full line,$\tilde{\nu}_{exc}$ = 31250 cm^{-1}) upon ligand-centered excitation (solid state, 77 K).

The replacement of the terminal diamagnetic Zn(II) with open-shell Cr(III) in $[CrGdCr(\mathbf{L2})_3]^{9+}$ enhances the paramagnetic coupling mechanism responsible for the increasing intensity of the spin-forbidden $^3\pi^*\rightarrow\pi$ phosphorescence[29] arising at 24 510 cm^{-1} (didentate unit, τ = 5.19(1) ms) and 21 050 cm^{-1} (tridentate unit, τ = 1.58(1) ms, Figure 5).

These spectroscopic levels are summarized in the associated Jablonski diagram (Figure 6, center), which can be completed with the Cr(^{2}E) excited state evidenced by intramolecular **L2**→Cr energy transfer processes sensitizing the famous long-lived Cr(^{2}E→^{4}A$_2$) luminescence at 13 240 cm^{-1} in $[CrGdCr(\mathbf{L2})_3]^{9+}$ ($\tau_{Cr(^2E)}^{CrGdCr} = 1/k_{Cr}^{CrGdCr}$ = 2.27(2) ms at 10 K, Table 1, column 2, Figure 5, and Figure S10).

The associated excitation profile recorded for $[CrGdCr(\mathbf{L2})_3]^{9+}$ upon monitoring the Cr(^{2}E→^{4}A$_2$) transition unravels that both Cr-centered Cr(^{2}E←^{4}A$_2$) at 13 330 cm^{-1}; Cr(^{2}T$_1$←^{4}A$_2$) at 13 910/14 090 cm^{-1}; Cr(^{4}T$_2$←^{4}A$_2$) at 19 970/21 780 cm^{-1} and ligand-centered (>24 500 cm^{-1}) excitation processes (Figure S11) contribute to NIR phosphorescence centered at 13 240 cm^{-1} (Figure 6). Because of the pseudo-D_3 symmetry in $[CrGdCr(\mathbf{L2})_3]^{9+}$, the Cr(^{4}T$_2$) and Cr(^{2}T$_1$) excited levels are split into A + E components. From the barycenter of these transitions, we can estimate the Cr(III) pseudo-octahedral ligand-field strength Δ = 20 880 cm^{-1}[12–14] and the Racah parameter B = 750 cm^{-1}, that is reduced to 72% of its free ion value by the nephelauxetic effect; see eq 3 with $C \approx 4B$ for N-donor atoms bound to Cr(III).[30]

dx.doi.org/10.1021/ja304009b | J. Am. Chem. Soc. 2012, 134, 12675–12684

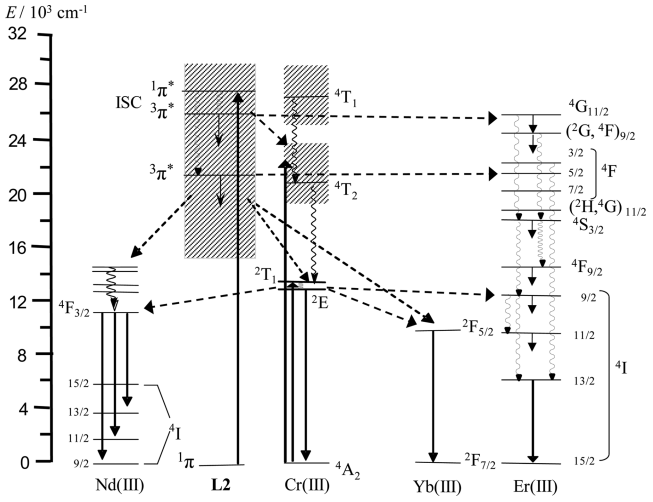

Figure 6. Partial energy level diagram with pertinent excited states for individual components summarizing the excitation processes (straight upward arrows), resonant energy transfer processes (horizontal dashed arrows), phonon-assisted energy transfer processes (diagonal dashed arrows), nonradiative multiphonon relaxation (undulating arrows), and observed radiative emission processes (straight downward arrows) occurring in $[ZnLnZn(\mathbf{L2})_3](CF_3SO_3)_7$ and $[CrLnCr(\mathbf{L2})_3](CF_3SO_3)_9$ (Ln = Nd, Er, Yb). The $Cr(^2T_2)$ levels are omitted for clarity, although they can act as a relay for energy transfer processes.

$$\Delta E = E[Cr(^2E)] - E[Cr(^4A_2)] = (9B + 3C - 90B^2/\Delta) = 13\,330 cm^{-1} \quad (3)$$

The energies of the Ln-centered excited levels are deduced from excitation of the ligand-centered $^1\pi^*$ singlet states in $[ZnLnZn(\mathbf{L2})_3]^{7+}$ (Ln = Nd, Er, Yb), which produces residual ligand-centered emission because of incomplete **L2**→Ln(III) energy transfer, together with Ln-centered luminescence assigned to specific 4f–4f transitions (Figure 6 and Figure S12).[31] The characteristic lifetimes of the Ln-centered NIR emissions are within the microsecond range as expected for molecular complexes with reasonably protected coordination sites ($\tau^{ZnNdZn}_{Nd(^4F_{3/2})} = 1/k^{ZnNdZn}_{Nd} = 1.60(6)$ μs, $\tau^{ZnErZn}_{Er(^4I_{13/2})} = 1/k^{ZnErZn}_{Er} = 4.54(4)$ μs, and $\tau^{ZnYbZn}_{Yb(^2F_{5/2})} = 1/k^{ZnYbZn}_{Yb} = 31.0(2)$ μs, solid state 10 K, Table 1, column 4).[9]

Finally, irradiation into the ligand-centered $\pi\rightarrow\pi^*$ transitions in $[CrLnCr(\mathbf{L2})_3]^{9+}$ (Ln = Nd, Er, Yb) induces a luminescence produced by three components: (i) the residual ligand-centered $^3\pi^*\rightarrow\pi$ phosphorescence (incomplete **L2**→Cr, Ln energy transfers), (ii) the Cr(III) sensitized emission at 13 300 cm^{-1}; and (iii) the Ln(III) sensitized NIR emission at ∼10 000 cm^{-1} for $Yb(^2F_{5/2}\rightarrow{}^2F_{7/2})$ (Figure 7), at ∼11 000/9500/7500 cm^{-1} for $Nd(^4F_{3/2}\rightarrow{}^4I_{9/2}, {}^4I_{11/2}, {}^4I_{13/2})$ (Figure S15a), and at ∼6500 cm^{-1} for $Er(^4I_{13/2}\rightarrow{}^4I_{15/2})$ (Figure S15b). The excitation spectra recorded upon monitoring the Ln-centered NIR emission demonstrate that the $Cr(^2E)$ excited state can be systematically used as a feeding level for lanthanide sensitization in $[CrLnCr(\mathbf{L2})_3]^{9+}$ (Ln = Nd, Er, Yb, Figure S16). Consequently, selective laser excitation of the $Cr(^2E\leftarrow{}^4A_2)$ transition at 13 330 cm^{-1} produces dual emission arising from $Cr(^2E)/Nd(^4F_{3/2})$ in $[CrNdCr(\mathbf{L2})_3]^{9+}$, $Cr(^2E)/Er(^4I_{13/2})$ in $[CrErCr(\mathbf{L2})_3]^{9+}$, and $Cr(^2E)/Yb(^2F_{5/2})$ in $[CrYbCr(\mathbf{L2})_3]^{9+}$ with characteristic lifetimes $\tau^{CrLnCr}_{Cr(^2E)} = 1/k^{CrLnCr}_{Cr}$ and $\tau^{CrLnCr}_{Ln} = 1/k^{CrLnCr}_{Ln}$ collected in Table 1 (columns 3 and 5).

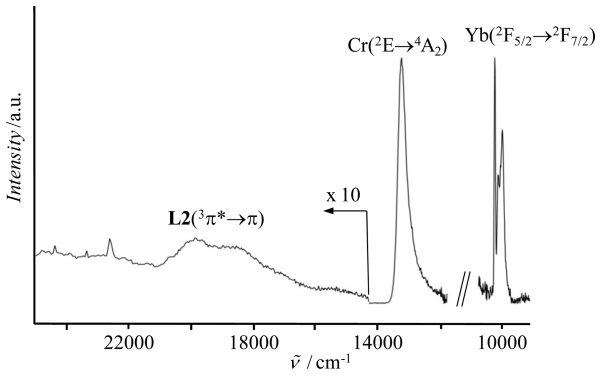

Figure 7. Emission spectrum recorded for $[CrYbCr(\mathbf{L2})_3](CF_3SO_3)_9$ upon ligand-centered excitation ($\tilde{\nu}_{exc}$ = 37 037 cm^{-1}, solid state, 77 K).

Intermetallic Energy Transfer and Light-Conversion Processes in $[CrLnCr(L2)_3](CF_3SO_3)_9$ (Ln = Nd, Er, Yb). The use of short-time and low-power light pulses for pumping the $Cr(^2E\leftarrow{}^4A_2)$ transition in $[CrLnCr(\mathbf{L2})_3]^{9+}$ at 13 330 cm^{-1}

Table 1. Rate Constants (k/s^{-1}), Efficiencies (η, eq 5), Intramolecular Intermetallic Ln···Cr Distances ($R^{Cr,Ln}_{D,A}$/Å), and Critical Distances for 50% Energy Transfer ($R^{Cr,Ln}_0$/Å, eq 6) in $[LnCr(L1)_3]^{6+}$ and $[CrLnCr(L2)_3]^{9+}$ (Ln = Gd, Nd, Er, Yb; 10 K)[a]

compd	k^{CrGd}_{Cr}	k^{CrLn}_{Cr}	k^{ZnLn}_{Ln}	k^{CrLn}_{Ln}	$W_{Cr\rightarrow Ln}$	$\eta_{Cr\rightarrow Ln}$	$R^{Cr,Ln}_{D,A}$	$R^{Cr,Ln}_0$	ref
$[GdCr(\mathbf{L1})_3]^{6+}$	$2.73(8)\times10^2$								16
$[NdZn(\mathbf{L1})_3]^{6+}$			$6.85(5)\times10^5$						16
$[YbZn(\mathbf{L1})_3]^{6+}$			$5.0(3)\times10^4$						16
$[NdCr(\mathbf{L1})_3]^{6+}$		$2.13(7)\times10^3$		$2.1(3)\times10^3$	$1.86(8)\times10^3$	0.87(4)	9.28	12.8(2)	16
$[YbCr(\mathbf{L1})_3]^{6+}$		$5.1(2)\times10^2$		$5.0(5)\times10^2$	$2.4(1)\times10^2$	0.46(2)	9.33	9.1(1)	16
$[CrGdCr(\mathbf{L2})_3]^{9+}$	$4.40(9)\times10^2$								this work
$[ZnNdZn(\mathbf{L2})_3]^{9+}$			$6.2(1)\times10^5$						this work
$[ZnYbZn(\mathbf{L2})_3]^{9+}$			$3.2(1)\times10^4$						this work
$[ZnErZn(\mathbf{L2})_3]^{9+}$			$2.20(3)\times10^5$						this work
$[CrNdCr(\mathbf{L2})_3]^{9+}$		$2.00(6)\times10^3$		$4.0(4)\times10^3$	$1.56(6)\times10^3$	0.78(3)	8.9	11.0(1)	this work
$[CrYbCr(\mathbf{L2})_3]^{9+}$		$6.9(2)\times10^2$		$7.6(8)\times10^2$	$2.50(9)\times10^2$	0.36(2)	8.9	8.10(9)	this work
$[CrErCr(\mathbf{L2})_3]^{9+}$		$9.3(3)\times10^2$		$9.3(5)\times10^2$	$4.9(2)\times10^2$	0.53(3)	8.9	9.1(1)	this work

[a] k^{CrGd}_{Cr}, k^{CrLn}_{Cr}, k^{ZnLn}_{Ln}, and k^{CrLn}_{Ln} are reported with their experimental standard deviations. All other uncertainties are calculated by using standard mathematical propagations.[38]

dx.doi.org/10.1021/ja304009b | J. Am. Chem. Soc. 2012, 134, 12675–12684

produces a non-negligible transient population only for the lowest excited Cr*LnCr state ($|\alpha\rangle$ level in Figure 3b), which relaxes (i) via radiative and nonradiative pathways (k_{Cr}^{CrGdCr}) toward the CrLnCr ground state ($|0\rangle$ level in Figure 3b) and (ii) via energy transfer $W_{Cr\rightarrow Ln}^{CrLnCr}$ toward the CrLn*Cr state ($|\beta\rangle$ level in Figure 3b). This simple kinetic scheme allows straightforward estimates of energy transfer rate constants ($W_{Cr\rightarrow Ln}^{CrLnCr}$, eq 4) and efficiencies ($\eta_{Cr\rightarrow Ln}^{CrLnCr}$, eq 5) by using the experimental characteristic lifetimes of the $Cr(^2E)$ excited state measured for the isostructural $[CrGdCr(\mathbf{L2})_3]^{9+}$ ($\tau_{Cr(^2E)}^{CrGdCr}$) and $[CrLnCr(\mathbf{L2})_3]^{9+}$ ($\tau_{Cr(^2E)}^{CrLnCr}$) complexes (Ln = Nd, Er, Yb, Table 1).[12]

$$W_{Cr\rightarrow Ln}^{CrLnCr} = k_{Cr}^{CrLnCr} - k_{Cr}^{CrGdCr} = \left(\tau_{Cr(^2E)}^{CrLnCr}\right)^{-1} - \left(\tau_{Cr(^2E)}^{CrGdCr}\right)^{-1} \quad (4)$$

$$\eta_{Cr\rightarrow Ln}^{CrLnCr} = \frac{W_{Cr\rightarrow Ln}^{CrLnCr}}{W_{Cr\rightarrow Ln}^{CrLnCr} + k_{Cr}^{CrGdCr}} = 1 - \frac{k_{Cr}^{CrGdCr}}{k_{Cr}^{CrLnCr}} = 1 - \frac{\tau_{Cr(^2E)}^{CrLnCr}}{\tau_{Cr(^2E)}^{CrGdCr}} \quad (5)$$

The calculated rate constants for the intramolecular Cr→Ln energy transfer processes are similar for the dinuclear $[CrLn(\mathbf{L1})_3]^{6+}$ and trinuclear $[CrLnCr(\mathbf{L2})_3]^{9+}$ complexes (Ln = Nd, Yb, Table 1, column 6), in line with the starting hypothesis. This leads to slightly less efficient energy transfer for the latter complexes because of the shorter intrinsic $Cr(^2E)$ lifetime in $[CrGdCr(\mathbf{L2})_3]^{9+}$ (Table 1, columns 2 and 7). Although recent investigations[32] suggest that long-distance intermetallic d→f energy transfers may include a competition between the electron-exchange mechanism (i.e., Dexter-type)[33] and the (multipolar) Coulombic interaction between the donor and acceptor electric fields (i.e., Förster-type),[34] the energy transfer efficiencies in $[CrLn(\mathbf{L1})_3]^{6+}$ and $[CrLnCr(\mathbf{L2})_3]^{9+}$ (Ln = Nd, Er, Yb) were analyzed within the strict limit of the long-range dipole−dipole formalism according to eq 6, in which $R_{D,A}^{Ln,Cr}$ is the donor−acceptor distance separation taken as the intramolecular Cr···Ln contact distance in the complexes and $R_0^{Ln,Cr}$ is the critical distance at which $\eta_{Ln\rightarrow Cr} = 0.5$.[12,35] This simplification is justified by the presence of methylene units linking the three tridentate coordination moieties in **L2** acting as electronic insulators.

$$\eta_{Cr\rightarrow Ln} = \left[1 + \left(\frac{R_{D,A}^{Ln,Cr}}{R_0^{Ln,Cr}}\right)^6\right]^{-1} = \frac{(R_0^{Ln,Cr})^6}{(R_0^{Ln,Cr})^6 + (R_{D,A}^{Ln,Cr})^6} \quad (6)$$

We find critical distances for 50% energy transfer efficiencies in the nanometric range for all complexes with $R_0^{Nd,Cr} > R_0^{Er,Cr} > R_0^{Yb,Cr}$ (Table 1, column 9), a trend in line with the decreasing number of Ln-centered excited acceptor levels available on each cation for resonant or phonon-assisted energy transfer mechanisms (Figure 6).

We are now equipped for introducing the rate constants collected in Table 1 into eq 1 with the kinetic matrix adapted for $[CrLnCr(\mathbf{L2})_3]^{9+}$ (Figure S3a). Steady-state simulations for Ln = Nd, Er, Yb using the simplified Jablonski diagram depicted in Figure 3b show that the slow decay rates of the $Cr(^2E)$ donor levels control the stepwise depopulation of the CrLnCr ground state to the benefit of the Cr-centered excited levels Cr*LnCr (low pumping power) and Cr*LnCr* (large pumping power, Figure S17, Supporting Information). The population density of the Ln-centered NIR emitting levels CrLn*Cr, Cr*Ln*Cr, and Cr*Ln*Cr* remains negligible (less than 1%) for any pumping power leading to weak NIR emission because of the low intrinsic luminescence quantum efficiency of the Yb luminescence (Figure S18). We however could notice that the predicted statistical 2-fold gain in intensity in going from $[LnCr(\mathbf{L1})_3]^{6+}$ to $[CrLnCr(\mathbf{L2})_3]^{9+}$ is verified for Ln = Nd (Figure S19), whereas some "positive cooperative effect" is observed for Ln = Yb, with a somewhat larger overall gain (f_{gain} = 2.4 at low incident power and f_{gain} = 3.1 at high power, Figure 8). Interestingly, these slow Cr→Ln energy transfer rate

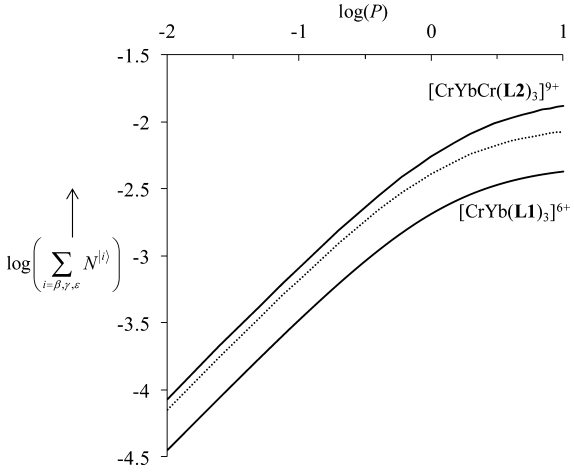

Figure 8. Computed linear dependences of Yb-centered emission intensity with respect to incident pump power (in W/mm^2) of the Cr-centered transitions in $[CrYb(\mathbf{L1})_3]^{6+}$ and $[CrYbCr(\mathbf{L2})_3]^{9+}$ (full traces, solid state, 10 K). The statistical behavior (f_{gain} = 2.0) predicted for $[CrYbCr(\mathbf{L2})_3]^{9+}$ by using the rate constants measured for $[CrYb(\mathbf{L1})_3]^{6+}$ is shown as a dotted trace.

constants can be converted into an advantage when one considers the apparent lifetimes of the Ln-centered NIR emission. For the short-time low-power light pulses used in this work, only the ground CrLnCr ($|0\rangle$) and the two first excited states Cr*LnCr ($|\alpha\rangle$) and CrLn*Cr ($|\beta\rangle$) contribute to the kinetic scheme. Equation 7 therefore satisfyingly models the relaxation processes originating from the initial density population matrix written as its transpose ($N_0^{|0\rangle} = (N_{tot} - N_0^{|\alpha\rangle})N_0^{|\alpha\rangle}N_0^{|\beta\rangle} = 0)^T$:

$$\begin{pmatrix} dN_t^{|0\rangle}/dt \\ dN_t^{|\alpha\rangle}/dt \\ dN_t^{|\beta\rangle}/dt \end{pmatrix} = \begin{pmatrix} 0 & k_{Cr}^{CrGdCr} & k_{Ln}^{ZnLnZn} \\ 0 & -(k_{Cr}^{CrGdCr} + W_{Cr\rightarrow Ln}) & 0 \\ 0 & W_{Cr\rightarrow Ln} & -k_{Ln}^{ZnLnZn} \end{pmatrix} \times \begin{pmatrix} N_t^{|0\rangle} \\ N_t^{|\alpha\rangle} \\ N_t^{|\beta\rangle} \end{pmatrix} \quad (7)$$

Using projection operator solutions,[20] we obtain (Appendix 1):

$$N_t^{|0\rangle} = N_{\text{tot}} - \frac{N_0^{|\alpha\rangle}}{(k_{\text{Ln}}^{\text{ZnLnZn}} - k_{\text{Cr}}^{\text{CrGdCr}} - W_{\text{Cr}\rightarrow\text{Ln}})} \left[(k_{\text{Ln}}^{\text{ZnLnZn}} - k_{\text{Cr}}^{\text{CrGdCr}})e^{-(k_{\text{Cr}}^{\text{CrGdCr}} + W_{\text{Cr}\rightarrow\text{Ln}})t} - W_{\text{Cr}\rightarrow\text{Ln}}e^{-k_{\text{Ln}}^{\text{ZnLnZn}}t}\right] \quad (8)$$

$$N_t^{|\alpha\rangle} = N_0^{|\alpha\rangle}e^{-(k_{\text{Cr}}^{\text{CrGdCr}} + W_{\text{Cr}\rightarrow\text{Ln}})t} \quad (9)$$

$$N_t^{|\beta\rangle} = \frac{W_{\text{Cr}\rightarrow\text{Ln}}N_0^{|\alpha\rangle}}{(k_{\text{Ln}}^{\text{ZnLnZn}} - k_{\text{Cr}}^{\text{CrGdCr}} - W_{\text{Cr}\rightarrow\text{Ln}})} \left[e^{-(k_{\text{Cr}}^{\text{CrGdCr}} + W_{\text{Cr}\rightarrow\text{Ln}})t} - e^{-k_{\text{Ln}}^{\text{ZnLnZn}}t}\right] \quad (10)$$

The time evolution of the population densities computed for $[\text{CrYbCr}(\mathbf{L2})_3]^{9+}$ (Figure 9), $[\text{CrNdCr}(\mathbf{L2})_3]^{9+}$ (Figure S20), and $[\text{CrErCr}(\mathbf{L2})_3]^{9+}$ (Figure S21) shows that, except for the first microseconds following the pulse, the decay rate of the Ln-centered NIR emission mirrors the $Cr(^2E)$ emission lifetimes and thus extends into the millisecond range. This prediction is confirmed by the apparent long experimental $Nd(^4F_{3/2})$, $Er(^4I_{13/2})$, and $Yb(^2F_{5/2})$ lifetimes observed in $[\text{CrLnCr}(\mathbf{L2})_3]^{9+}$ (Table 1, column 5).

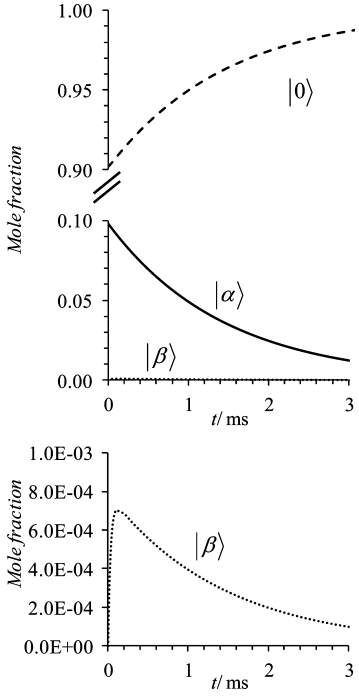

Figure 9. Computed time evolution of the population densities of the ground state CrYbCr ($|0\rangle$, dashed trace, eq 8), and of the lowest excited states Cr*YbCr ($|\alpha\rangle$, full trace, eq 9) and CrYb*Cr ($|\beta\rangle$, dotted trace, eq 10) in $[\text{CrYbCr}(\mathbf{L2})_3]^{9+}$ after a 500 μJ/mm^2 pulse in the Cr-centered transition (solid state, 10 K).

CONCLUSION

The connection of a second strong-field $[CrN_6]$ chromophore to the C_3-symmetrical dinuclear complexes $[\text{LnCr}(\mathbf{L1})_3]^{6+}$ resulting in the formation of $[\text{CrLnCr}(\mathbf{L2})_3]^{9+}$ does not significantly affect the ligand-centered and metal-centered photophysical properties. Excitation into the $Cr(^2E)$-centered levels with NIR irradiation at 13 300 cm^{-1} induces intramolecular Cr→Ln energy transfers, which eventually sensitize low-energy luminescence for Ln = Nd, Er, or Yb in the spectral range 6000−10 000 cm^{-1}. As compared to the fast Ln-centered relaxation pathways operating in $[\text{ZnLnZn}(\mathbf{L2})_3]^{9+}$, the slow Cr→Ln energy transfer responsible for the feeding of the same Ln-centered excited levels in $[\text{CrLnCr}(\mathbf{L2})_3]^{9+}$ acts as bottleneck, which controls the kinetics of the low-energy NIR emission. The apparent millisecond Ln-centered lifetimes thus mirror those of the $Cr(^2E)$ donor levels. This unusual property is obtained at the cost of the intensity of the NIR output, but the connection of a second Cr(III) donor in $[\text{CrLnCr}(\mathbf{L2})_3]^{9+}$ partially overcomes this limitation because the predicted intensities are more than twice larger than those found in the related dinuclear $[\text{LnCr}(\mathbf{L1})_3]^{6+}$ complexes. The effective experimental gain in NIR emission intensity further depends on the ratio between radiative and nonradiative de-excitation pathways for the emitting $Nd(^4F_{3/2})$, $Er(^4I_{13/2})$, and $Yb(^2F_{5/2})$ levels, a trend that can be addressed by measuring intrinsic and global quantum yields. Because no such data were recorded for $[\text{LnCr}(\mathbf{L1})_3]^{6+}$ in ref 23a, an exact comparison of experimental NIR→NIR light-conversion efficiencies between dinuclear and trinuclear complexes is currently inaccessible, but the encouraging global quantum yields measured for $[\text{CrLnCr}(\mathbf{L2})_3]^{9+}$ upon Cr-centered irradiation ($\eta_{\text{Nd}}^{\text{Cr}}$ = 0.027(1) and $\eta_{\text{Yb}}^{\text{Cr}}$ = 0.030(3), solid state, 295 K) are compatible with their use as long-lived NIR probes for analytical chemistry and biology. Last, but not least, the presence of two Cr(III) donors sandwiching the Ln(III) activator results in the non-negligible population of long-lived doubly excited states Cr*LnCr* ($|\delta\rangle$) and Cr*Ln*Cr ($|\gamma\rangle$, Figures 3b and S3) under reasonable pumping powers as illustrated for Yb on Figure 10 (see Figures S22−S23 for corresponding graphs for Nd and Er; equations are given in Appendix 2), a phenomenon that has no counterpart in the parent dinuclear complexes (Figure 2).

This work opens unprecedented perspectives for the programming of molecular Ln-centered energy transfer upconversion (ETU) processes exploiting lanthanide-centered CrLn**Cr doubly excited states when the activator possesses an adequate series of accessible spectroscopic levels as found in $[\text{CrErCr}(\mathbf{L2})_3]^{9+}$.[23b] We believe that such a supramolecular control of NIR luminescence parameters will be helpful for the design of materials and probes in fields as diverse as telecommunications, security devices, and bioimaging, especially that extension to multidimensional arrays can be envisaged.[36]

EXPERIMENTAL SECTION

Synthesis. Chemicals were purchased from Strem, Acros, Fluka AG, and Aldrich, and used without further purification unless otherwise stated. The ligand **L2**[37] and complexes $Cr(CF_3SO_3)_2{\cdot}H_2O$,[23a] $[\text{ZnGdZn}(\mathbf{L2})_3](CF_3SO_3)_7$,[23a] $[\text{CrGdCr}(\mathbf{L2})_3](CF_3SO_3)_9$,[23a] and $[\text{CrErCr}(\mathbf{L2})_3](CF_3SO_3)_9$[23b] were prepared according to literature procedures. The triflate salts $Ln(CF_3SO_3)_3{\cdot}nH_2O$ were prepared from the corresponding oxide (Aldrich, 99.99%).[39] Acetonitrile and dichloromethane were distilled over calcium hydride.

Preparation of $[ZnLnZn(\mathbf{L2})_3](CF_3SO_3)_7{\cdot}nH_2O$ (Ln = Nd, Er, Yb). $Ln(CF_3SO_3)_3{\cdot}xH_2O$ (17 μmol) in acetonitrile (2 mL) was added into a dichloromethane/acetonitrile (1:1, 24 mL) solution of **L2** (41.3 mg, 51 μmol). After being stirred at room temperature for 24 h, the mixture was evaporated to dryness, the solid residue was dissolved into acetonitrile (10 mL), and $Zn(CF_3SO_3)_2$ (12.4 mg, 34 μmol) in acetonitrile (2 mL) was added. The resulting solution was stirred for 24 h and concentrated. Slow diffusion of diethylether (12 h) eventually

dx.doi.org/10.1021/ja304009b | J. Am. Chem. Soc. 2012, 134, 12675−12684

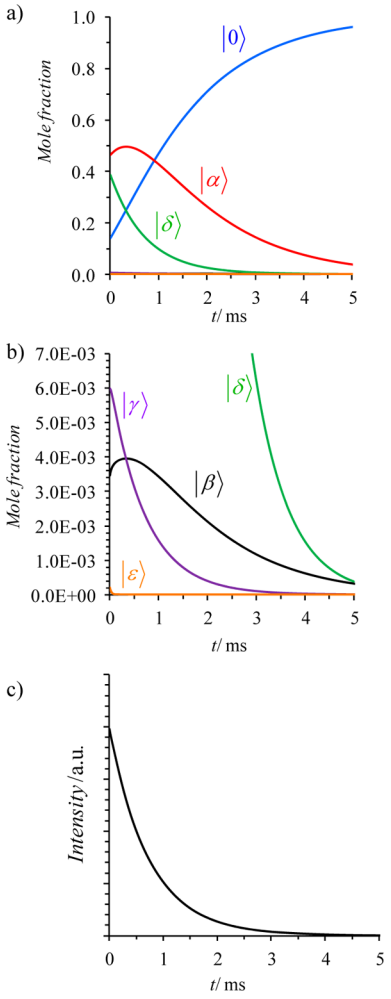

Figure 10. (a) 0−1.0 mol fraction and (b) 0−0.007 mol fraction time evolution of the population densities for the ground state CrYbCr ($|0\rangle$, blue trace) and of the excited states Cr*YbCr ($|\alpha\rangle$, red trace), CrYb*Cr ($|\beta\rangle$, black trace), Cr *Yb*Cr ($|\gamma\rangle$, violet trace), Cr*YbCr* ($|\delta\rangle$, green trace), and Cr*Yb*Cr* ($|\varepsilon\rangle$, orange trace) in $[CrYbCr(\mathbf{L2})_3]^{9+}$ and (c) Yb-centered emission intensity following a 3 W/mm^2 photonic presaturation (solid state, 10 K, eq S13).

gave 75−80% $[ZnLnZn(\mathbf{L2})_3](CF_3SO_3)_7{\cdot}nH_2O$ (Ln = Nd, Er, Yb) as yellow microcrystals, which were characterized by ^{1}H NMR, ESI-MS, and elemental analyses (Table S1).

Preparation of $[CrLnCr(\mathbf{L2})_3](CF_3SO_3)_9{\cdot}m$TBAf$\cdot nH_2O$ (Ln = Nd, Er, Yb). $Ln(CF_3SO_3)_3{\cdot}xH_2O$ (17 μmol) in acetonitrile (2 mL) was added into a dichloromethane/acetonitrile (1:1, 24 mL) solution of **L2** (41.3 mg, 51 μmol). After being stirred at room temperature for 24 h, the mixture was evaporated to dryness, and the pale yellow solid was transferred into a glovebox and dissolved in degassed acetonitrile (25 mL). A blue degassed acetonitrile solution (1 mL) of $Cr(CF_3SO_3)_2{\cdot}1H_2O$ (12.6 mg, 34 μmol) was added, and the resulting mixture slowly turned brown, then green. After being stirred for 12 h under an inert atmosphere, solid $Bu_4NCF_3SO_3$ (TBAf, 13.3 mg, 34 μmol) was added and air was slowly bubbled through the solution for 2 h. The yellow solution was evaporated, and the solid residue was dissolved in a minimum amount of acetonitrile. Slow diffusion of diethyl ether (24 h) yielded 92−95% of $[CrLnCr(\mathbf{L2})_3](CF_3SO_3)_9{\cdot}m$TBAf$\cdot nH_2O$ (Ln = Nd, Er, Yb) as pale microcrystalline powders, which were separated by filtration, washed with diethylether, dried under vacuum, and characterized by ESI-MS and elemental analyses (Table S1). Slow diffusion of diethylether into a concentrated propionitrile solution of $[CrYbCr(\mathbf{L2})_3](CF_3SO_3)_9{\cdot}0.5$TBAf$\cdot 3H_2O$ gave fragile X-ray quality prisms of $[CrYbCr(\mathbf{L2})_3](CF_3SO_3)_9(C_3H_5N)_{30}$.

Spectroscopic Measurements. ^{1}H NMR spectra were recorded at 298 K on a Bruker Avance 400 MHz spectrometer. Chemical shifts were given in ppm with respect to TMS. Pneumatically assisted electrospray (ESI-MS) mass spectra were recorded from 3 to 5×10^{-4} M solutions on an Applied Biosystems API 150EX LC/MS System equipped with a Turbo Ionspray source, on a Finnigan-mat SSQ 7000, or on an Applied Biosystem API III. Elemental analyses were performed by Dr. H. Eder from the Microchemical Laboratory of the University of Geneva. Electronic spectra in the UV−vis were recorded at 293 K from solutions in MeCN with a Perkin-Elmer Lambda 900 spectrometer using quartz cells of 0.1 cm path length.

Photophysical investigations at 10 K were performed on powdered samples, which were mounted onto copper plates with either rubber cement or conductive silver glue; cooling was achieved either with a closed-cycle He cryostat (CTI-Cryogenics, Oxford Instruments, CCC1100T) or with a liquid-helium bath cryostat (Oxford Instruments MD4). For room temperature or 77 K measurements, the samples were transferred into quartz tubes ($Ø_{in}$ = 2.4 mm, Verre et Quartz Technique SA, Neuchâtel) or borosilicate glass tubes (Ø = 0.8−1.1 mm, Kimble Kontes), which were sealed with Parafilm. Room temperature and 77 K emission and excitation spectra were measured on a LS-50B fluorescence spectrometer (Perkin-Elmer) or a Fluorolog FL3-22 spectrometer (Horiba Jobin-Yvon Ltd.) equipped with a 450W Xe-lamp, two double-grating emission monochromators, and three different detectors, a Hamamatsu R928 photomultiplier (300−750 nm), a solid-state InGaAs detector cooled at 77 K (range 800−1600 nm), and a Peltier-cooled (−60 °C) Hamamatsu H9170-75 photomultiplier (950−1700 nm) for measuring the $Er^{3+}(^4I_{13/2} \rightarrow {}^4I_{15/2})$ emission. High-resolution room temperature and low temperature emission spectra were recorded upon excitation with an Ar^+ laser (Coherent Innova 90C) at 488 nm or with Nd:YAG laser (Quantel Brillant B) at 355 nm. The emitted light was analyzed at 90° with a Spex 270 M monochromator blazed at 600 nm with holographic gratings (150 L/mm). Light intensity was measured by a photomultiplier or CCD detectors. Appropriate filters were utilized to remove the laser light, the Rayleigh scattered light, and associated harmonics from the emission spectra. Luminescent lifetimes were measured using excitation provided by a Quantum Brillant or Quantel YG 980 Nd:YAG laser equipped with frequency doubler, tripler, and quadrupler as well as with an OPOTEK MagicPrismTM OPO crystal and a Quantel TDL + dye laser. The output signal of the photomultiplier was fed into a Stanford Research SR-400 multichannel scaler or to a 500 MHz Tektronics TDS724C and transferred to a PC for treatment with Origin 8. Lifetimes are averages of three independent determinations. Resonant excitation into the $Cr(^2E \leftarrow {}^4A_2)$ transition in CrLnCr was achieved with a tunable Ti:sapphire laser (Spectra Physics 3900S) pumped by the 532 nm excitation of a Nd:YVO_4 laser (Spectra Physics Millenia-10SJ). The excitation was tuned to 13 360−13 890 cm^{-1}. A short pass filter that cuts the scattered laser light and allows the passing of green light was used for these measurements. Residual pump laser light was removed at the exit of the Ti:sapphire laser with an RG 715 nm color filter. All excitation spectra were corrected for the emission of the xenon lamp, and all emission spectra were corrected for the instrumental response. The spectra were displayed as photons versus energy (cm^{-1}). Quantum yield measurements of the solid state samples were measured on quartz tubes with the help of an integration sphere developed by Frédéric Gumy at the Laboratory of Lanthanide Supramolecular Chemistry, EPFL) and commercialized by GMP S.A. (Renens, Switzerland, www.gmp.ch).[40]

Computational Details. The gas-phase geometry of the complex $[ZnEuZn(\mathbf{L2})_3]^{7+}$ was optimized by Density Functional Theory using the PW91PW91 exchange-correlation functional[41] implemented in Gaussian 03.[42] The DZVP double-ζ basis set developed by Godbout et al.[43] was used for the H, C, N, and Zn atoms, and the europium cation was described by the quasi-relativistic pseudopotential of Dolg et al.[44] for the 52 + 4f^n core electrons and by a (7s, 6p, 5d)/(5s, 4p, 3d)

Gaussian basis set for the valence electrons. All kinetic calculations were performed with EXCEL.

■ ASSOCIATED CONTENT

Supporting Information

Details for the determination of matrix differential equations (appendices 1 and 2); tables of ^{1}H NMR shifts, elemental analyses, ESI-MS molecular peaks, characteristic emission lifetimes; figures showing ^{1}H NMR spectra, ESI-MS spectra, molecular structure models, computed steady-state and time-evolution of population densities, computed dependences of the intensity on the incident pump power, electronic excitation and emission spectra, and Tanabe–Sugano diagram. This material is available free of charge via the Internet at http://pubs.acs.org.

■ AUTHOR INFORMATION

Corresponding Author

claude.piguet@unige.ch; jean-claude.bunzli@epfl.ch; andreas.hauser@unige.ch; stephane.petoud@cnrs-orleans.fr

Notes

The authors declare no competing financial interest.

■ ACKNOWLEDGMENTS

Financial support from the Swiss National Science Foundation is gratefully acknowledged. S.P. acknowledges support in France from la Ligue contre le Cancer and from Institut National de la Santé et de la Recherche Médicale (INSERM). J.-C.G.B. thanks the world Class University program (Photovoltaic Materials) funded by the Ministry of Education, Science, and Technology of the South Korean government (grant R31-2011-000-10035-0).

■ REFERENCES

(1) (a) Carnall, W. T.; Hessler, J. P.; Wagner, F. J. *J. Chem. Phys.* **1968**, *49*, 4424–4442. (b) Carnall, W. T. In *Handbook on the Physics and Chemistry of Rare Earths*; Gschneidner, K. A., Jr., Eyring, L., Eds.; North Holland, Amsterdam, 1979; Vol. 3, pp 172–208.

(2) Kuriki, K.; Koike, Y.; Okamoto, Y. *Chem. Rev.* **2002**, *102*, 2347–2356.

(3) (a) Reisfeld, R.; Jørgensen, C. K. *Lasers and Excited States of Rare Earths*; Springer-Verlag: Berlin, Heidelberg, New York, 1977. (b) Kido, J.; Okamoto, Y. *Chem. Rev.* **2002**, *102*, 2357–2368.

(4) Auzel, F. *Chem. Rev.* **2004**, *104*, 139–173.

(5) (a) Weissleder, R.; Ntziachristos, V. *Nat. Med.* **2003**, *9*, 123–128. (b) Kim, S.; Lim, Y. T.; Soltesz, E. G.; De Grand, A. M.; Lee, J.; Nakayama, A.; Parker, J. A.; Mihaljevic, T.; Laurence, R. G.; Dor, D. M.; Cohn, H.; Bawendi, M. G.; Frangioni, J. V. *Nat. Biotechnol.* **2004**, *22*, 93–97. (c) Kamura, M.; Kanayama, N.; Tokuzen, K.; Soga, K.; Nagasaki, Y. *Nanoscale* **2011**, *3*, 3705–13. (d) Werts, M. H. V. In *Lanthanide Luminescence: Photophysical, Analytical, and Biological Aspects*; Springer Series on Fluorescence; Hänninen, P., Härmä, H., Eds.; Springer Verlag: New York, 2011; Vol. 7, Chapter 5, pp 136–159. (e) Pansare, V. J.; Hejazi, S.; Faenza, W. J.; Prud'homme, R. K. *Chem. Mater.* **2012**, *24*, 812–827.

(6) (a) Comby, S.; Bünzli, J.-C. G. In *Handbook on the Physics and Chemistry of Rare Earths*; Gschneidner, K. A., Jr., Bünzli, J.-C. G., Pecharsky, V. K., Eds.; Elsevier Science: Amsterdam, 2007; Vol. 37, pp 217–470. (b) Wong, W.-K.; Zhu, X.; Wong, W.-Y. *Coord. Chem. Rev.* **2007**, *251*, 2386–2399. (c) Zhu, X.; Wong, W.-K.; Wong, W.-Y.; Yang, X. *Eur. J. Inorg. Chem.* **2011**, 4651–4674.

(7) (a) Albrecht, M.; Fiege, M.; Osetska, O. *Coord. Chem. Rev.* **2008**, *252*, 812–824. (b) Petoud, S. *Chimia* **2009**, *63*, 745–752. (c) Zhong, Y.; Si, L.; He, H.; Sykes, A. G. *Dalton Trans.* **2011**, *40*, 11389–11395. (d) Artizzu, F.; Mercuri, M. L.; Serpe, A.; Deplano, P. *Coord. Chem. Rev.* **2011**, *255*, 2514–2529.

(8) (a) Ziessel, R. F.; Ulrich, G.; Charbonnière, L. J.; Imbert, C.; Scopelliti, R.; Bünzli, J.-C. G. *Chem.-Eur. J.* **2006**, *12*, 5060–5067. (b) Moore, E. G.; Xu, J.; Dodani, S. C.; Jocher, C. J.; D'Aléo, A.; Seitz, M.; Raymond, K. N. *Inorg. Chem.* **2010**, *49*, 4156–4166.

(9) Reinhard, C.; Güdel, H. U. *Inorg. Chem.* **2002**, *41*, 1048–1055.

(10) Imbert, D.; Cantuel, M.; Bünzli, J.-C. G.; Bernardinelli, G.; Piguet, C. *J. Am. Chem. Soc.* **2003**, *125*, 15698–15699.

(11) (a) Ward, M. D. *Coord. Chem. Rev.* **2007**, *251*, 1663–1677. (b) Ward, M. D. *Coord. Chem. Rev.* **2010**, *254*, 2634–2642. (c) Chen, F.-F.; Chen, Z.-Q.; Bian, Z.-Q.; Huang, C.-H. *Coord. Chem. Rev.* **2010**, *254*, 991–1010.

(12) Aboshyan-Sorgho, L.; Cantuel, M.; Petoud, S.; Hauser, A.; Piguet, C. *Coord. Chem. Rev.* **2012**, *256*, 1644–1663.

(13) (a) Kirk, A. D. *Chem. Rev.* **1999**, *99*, 1607–1640. (b) Wagenknecht, P. S.; Ford, P. C. *Coord. Chem. Rev.* **2011**, *255*, 591–616.

(14) $\tilde{\nu}_{MLCT}$ = 38 600 cm^{-1}, $\tilde{\nu}(^4T_1 \leftarrow {}^4A_2)$ = 32 600 cm^{-1}, $\tilde{\nu}(^4T_2 \leftarrow {}^4A_2)$ = 26 700 cm^{-1}, $\tilde{\nu}(^2E \leftarrow {}^4A_2)$ = 12 370 cm^{-1}. (a) Lever, A. B. P. *Inorganic Electronic Spectroscopy*, 2nd ed.; Elsevier: Amsterdam, The Netherlands, 1984. (b) Ryu, C. K.; Endicott, J. F. *Inorg. Chem.* **1988**, *27*, 2203–2214.

(15) Lazarides, T.; Davies, G. M.; Adams, H.; Sabatini, C.; Barigelletti, F.; Barbieri, A.; Pope, S. J. A.; Faulkner, S.; Ward, M. D. *Photochem. Photobiol. Sci.* **2007**, *6*, 1152–1157.

(16) Torelli, S.; Imbert, D.; Cantuel, M.; Bernardinelli, G.; Delahaye, S.; Hauser, A.; Bünzli, J.-C. G.; Piguet, C. *Chem.-Eur. J.* **2005**, *11*, 3228–3242.

(17) (a) Subhan, M. A.; Suzuki, T.; Kaizaki, S. *J. Chem. Soc., Dalton Trans.* **2001**, 492–497. (b) Subhan, M. A.; Suzuki, T.; Kaizaki, S. *J. Chem. Soc., Dalton Trans.* **2002**, 1416–1422. (c) Subhan, M. A.; Nakata, H.; Suzuki, T.; Choi, J.-H.; Kaizaki, S. *J. Lumin.* **2003**, *101*, 307–315. (d) Subhan, M. A.; Kawahata, R.; Nakata, H.; Fuyuhiro, A.; Tsukuda, T.; Kaizaki, S. *Inorg. Chim. Acta* **2004**, *357*, 3139–3146.

(18) (a) Cantuel, M.; Bernardinelli, G.; Imbert, D.; Bünzli, J.-C. G.; Hopfgartner, G.; Piguet, C. *J. Chem. Soc., Dalton Trans.* **2002**, 1929–1940. (b) Cantuel, M.; Bernardinelli, G.; Muller, G.; Riehl, J. P.; Piguet, C. *Inorg. Chem.* **2004**, *43*, 1840–1849. (c) Telfer, S. G.; Tajima, N.; Kuroda, R.; Cantuel, M.; Piguet, C. *Inorg. Chem.* **2004**, *43*, 5302–5310.

(19) For the sake of clarity, we exclude in Figure 2 the case of direct $Cr(^2E \leftarrow {}^4A_2)$ irradiation, for which additional stimulated emissions should be considered.

(20) Starzak, M. E. *Mathematical Methods in Chemistry and Physics*; Plenum Press: New York and London, 1989; Chapters 6 and 9.

(21) Pollnau, M.; Gamelin, D. R.; Lüthi, S. R.; Güdel, H. U. *Phys. Rev.* **2000**, *B61*, 3337–3346.

(22) In cm^2 unit, $\sigma_{Cr} = 3.8 \times 10^{-21} \cdot \varepsilon$ for the molar absorption coefficient ε taken in M^{-1} cm^{-1}.

(23) (a) Cantuel, M.; Gumy, F.; Bünzli, J.-C. G.; Piguet, C. *Dalton Trans.* **2006**, 2647–2660. (b) Aboshyan-Sorgho, L.; Besnard, C.; Pattison, P.; Kittilstved, K. R.; Aebischer, A.; Bünzli, J.-C. G.; Hauser, A.; Piguet, C. *Angew. Chem., Int. Ed.* **2011**, *50*, 4108–4112.

(24) (a) Bertini, I.; Luchinat, C. *Coord. Chem. Rev.* **1996**, *150*, 1–292. (b) Bertini, I.; Fragai, M.; Luchinat, C.; Parigi, G. *Inorg. Chem.* **2001**, *40*, 4030–4035.

(25) The crystal structures of $[CrLnCr(\mathbf{L2})_3](CF_3SO_3)_9(C_3H_5N)_{30}$ (Ln = Eu: CCDC-806425 and Ln = Yb: CCDC-806426) have been previously reported in a preliminary communication.[23b]

(26) Piguet, C.; Bünzli, J.-C. G.; Bernardinelli, G.; Hopfgartner, G.; Petoud, S.; Schaad, O. *J. Am. Chem. Soc.* **1996**, *118*, 6681–6697.

(27) Whereas Zn(II) is a closed-shell cation with a non-degenerated ^{1}S spectroscopic term, Gd(III) is paramagnetic, but its first excited state $^6P_{7/2}$ is located 32 000 cm^{-1} above the ground state $^8S_{7/2}$, and it therefore cannot contribute to the photophysical response upon visible excitation. Carnall, W. T.; Fields, P. R.; Rajnak, K. *J. Chem. Phys.* **1968**, *49*, 4443–4446.

(28) (a) Davydov, A. S. *Theory of Absorption of Light in Molecular Crystals*; Ukrainian Academy of Sciences: Kiev, 1951. (b) Nakamoto, K. *J. Phys. Chem.* **1960**, *64*, 1420−1425. (c) Kasha, M.; Oppenheimer, M. *Theory of Molecular Excitons*; McGraw-Hill Book Co. Inc.: New York, 1962. (d) Telfer, S. G.; McLean, T.; Waterland, M. R. *Dalton Trans.* **2011**, *40*, 3097−3108.

(29) (a) Tobita, S.; Arakawa, M.; Tanaka, I. *J. Phys. Chem.* **1984**, *88*, 2697−2702. (b) Tobita, S.; Arakawa, M.; Tanaka, I. *J. Phys. Chem.* **1985**, *89*, 5649−5654.

(30) (a) Witzke, H. *Theor. Chim. Acta* **1971**, *20*, 171−185. (b) Trueba, A.; Garcia-Fernandez, P.; Garcia-Lastra, J. M.; Aeramburu, J. A.; Barriuso, M. T.; Moreno, M. *J. Phys. Chem. A* **2011**, *115*, 1423−1432. As compared to $[Cr(2,2'\text{-dipyridine})_3]^{3+}$ (Δ = 23 240 cm^{-1}, B = 761 cm^{-1}),[14] the spectroscopic parameters found for $[CrGd(\mathbf{L1})_3]^{6+}$ (Δ = 21 000 cm^{-1}, B = 747 cm^{-1})[12] and for $[CrGdCr(\mathbf{L2})_3]^{9+}$ (Δ = 20 880 cm^{-1}, B = 750 cm^{-1}) indicate that the terminal didentate 2-pyridyl-benzimidazole unit in **L1** and **L2** is a weaker σ-donor and a stronger π-acceptor.

(31) The analysis of high-resolution emission spectra for $[ZnLnZn(\mathbf{L2})_3]^{7+}$ (Ln = Nd, Yb, Figure S13) leads to the identification of ligand-field sublevels (Figure S14), from which we deduce that the crystal field effects in $[ZnLnZn(\mathbf{L2})_3]^{7+}$ are identical, within 10 cm^{-1}, with those reported for $[LnZn(\mathbf{L1})_3]^{5+}$ despite the replacement of LnN_6O_3 with LnN_9 coordination spheres.[16]

(32) Lazarides, T.; Sykes, D.; Faulkner, S.; Barbieri, A.; Ward, M. D. *Chem.-Eur. J.* **2008**, *14*, 9389−9399.

(33) Dexter, D. L. *J. Chem. Phys.* **1953**, *21*, 836−850.

(34) (a) Förster, T. *Ann. Phys.* **1948**, *2*, 55−75. (b) Förster, T. *Discuss. Faraday Soc.* **1959**, *27*, 7−17. (c) Förster, T. *Comparative Effects of Radiation*; Burton, M., Kirby-Smith, J. S., Magee, J. L., Eds.; John Wiley & Sons, Inc.: New York, 1960; pp 300−319.

(35) (a) Bünzli, J.-C. G. In *Lanthanide Probes in Life, Chemical and Earth Sciences*; Choppin, G., Bünzli, J.-C. G., Eds.; Elsevier: Amsterdam, 1989; Chapter 7. (b) Langford, V. S.; von Arx, M. E.; Hauser, A. *J. Phys. Chem. A* **1999**, *103*, 7161−7169.

(36) Aroussi, B. E.; Zebret, S.; Besnard, C.; Perrottet, P.; Hamacek, J. *J. Am. Chem. Soc.* **2011**, *133*, 10764−10767.

(37) Piguet, C.; Bocquet, B.; Hopfgartner, G. *Helv. Chim. Acta* **1994**, *77*, 931−942.

(38) Skoog, D. A.; West, D. M.; Holler, F. J.; Crouch, S. R. *Fundamentals of Analytical Chemistry*, 8th ed.; Brooks Cole: 2003; Chapter 3.

(39) Desreux, J. F. In *Lanthanide Probes in Life, Chemical and Earth Sciences*; Choppin, G., Bünzli, J.-C. G., Eds.; Elsevier: Amsterdam, 1989; Chapter 2.

(40) Aebischer, A.; Gumy, F.; Bünzli, J.-C. G. *Phys. Chem. Chem. Phys.* **2009**, *11*, 1346−1353.

(41) Perdew, J. P.; Burke, K.; Wang, Y. *Phys. Rev. B* **1996**, *54*, 16533−16539.

(42) Frisch, M. J.; Trucks, G. W.; Schlegel, H. B.; Scuseria, G. E.; Robb, M. A.; Cheeseman, J. R.; Montgomery, J. A., Jr.; Vreven, T.; Kudin, K. N.; Burant, J. C.; Millam, J. M.; Iyengar, S. S.; Tomasi, J.; Barone, V.; Mennucci, B.; Cossi, M.; Scalmani, G.; Rega, N.; Petersson, G. A.; Nakatsuji, H.; Hada, M.; Ehara, M.; Toyota, K.; Fukuda, R.; Hasegawa, J.; Ishida, M.; Nakajima, T.;. Honda, Y.; Kitao, O.; Nakai, H.; Klene, M.; Li, X.; Knox, J. E.; Hratchian, H. P.; Cross, J. B.; Bakken, V.; Adamo, C.; Jaramillo, J.; Gomperts, R.; Stratmann, R. E.; Yazyev, O.; Austin, A. J.;. Cammi, R.; Pomelli, C.; Ochterski, J. W.; Ayala, P. Y.; Morokuma, K.; Voth, G. A.; Salvador, P.; Dannenberg, J. J.; Zakrzewski, V. G.; Dapprich, S.; Daniels, A. D.; Strain, M. C.; Farkas, O.; Malick, D. K.; Rabuck, A. D.; Raghavachari, K.; Foresman, J. B.; Ortiz, J. V.; Cui, Q.; Baboul, A. G.; Clifford, S.; Cioslowski, J.; Stefanov, B. B.; Liu, G.; Liashenko, A.; Piskorz, P.; Komaromi, I.; Martin, R. L.; Fox, D. J.; Keith, T.; Al-Laham, M. A.; Peng, C. Y.; Nanayakkara, A.; Challacombe, M.; Gill, P. M. W.; Johnson, B.; Chen, W.; Wong, M. W.; Gonzalez, C.; Pople, J. A. *Gaussian 03*, revision B.03; Gaussian, Inc.: Wallingford, CT, 2004.

(43) Godbout, N.; Salahub, D. R.; Andzelm, J.; Wimmer, E. *Can. J. Chem.* **1992**, *70*, 560−571.

(44) Dolg, M.; Stoll, H.; Savin, A.; Preuss, H. *Theor. Chim. Acta* **1989**, *75*, 173−194. Dolg, M.; Stoll, H.; Preuss, H. *Theor. Chim. Acta* **1993**, *85*, 441−450.

Optimizing Millisecond Timescale Near-infrared Emission in Polynuclear Chrome(III)-Lanthanide(III) Complexes.

Lilit Aboshyan Sorgho, Homayoun Nozary, Annina Aebischer, Jean-Claude G. Bünzli,* Pierre-Yves Morgantini, Kevin R. Kittilstved, Andreas Hauser,* Svetlana V. Eliseeva, Stéphane Petoud* and Claude Piguet*

Supporting Information

(33 pages)

X-Ray Crystallography.[23b]

Extensive tabular information concerning the crystal structures of $[CrEuCr(\mathbf{L2})_3](CF_3SO_3)_9(C_2H_5N)_{30}$ (CCDC-806425) and $[CrYbCr(\mathbf{L2})_3](CF_3SO_3)_9(C_2H_5N)_{30}$ (CCDC-806426) can be found in reference 23b. The cif files can be obtained free of charge via www.ccdc.cam.ac.uk/conts/retrieving.html (or from the Cambridge Crystallographic Data Centre, 12 Union Road, Cambridge CB2 1EZ, UK; fax: (+ 44) 1223-336-033; or deposit@ccdc.cam.ac.uk). Due to the disorder exhibited by solvent molecules and by the counter-anions, the high-angle data were of low quality and the data were cut to a resolution of 0.95 Å for the CrEuCr compound and 1.1 Å for the CrYbCr compound. Among the eighteen triflate anions, fifteen were localized for CrEuCr and thirteen for CrYbCr**.** Restraints were applied on their C-S, S-O, C-F bond length, on the internal triflate bond angles and on their anisotropic displacement parameters. For CrYbCr restraints were also applied on some bond lengths of the ligands. For both compounds, the anisotropic displacement parameters of the ligands were restrained. Seven planar aromatic groups were defined for each ligand and similitude restraints were applied within the groups. Of the 2889 restraints used for CrEuCr, 77 corresponded to geometrical parameters (triflates), whereas 2812 concerned anisotropic displacement parameters. For CrYbCr, 487 constraints were applied on geometrical parameters (triflates and ligands), whereas 2238 constraints concerned the anisotropic displacement parameters. The interstitial solvent molecules were disordered and the"SQUEEZE/BYPASS" procedure was used within PLATON.[S1] Using this procedure, 4538 electrons located in a void of 18190 $Å^3$ were accounted for in the case of CrEuCr, while 5590 electrons located in a void of 19999 $Å^3$ were accounted for in the case of CrYbCr. These electrons were assigned to the missing triflate molecules required for neutrality and to the disordered acetonitrile solvent molecules. Figures S7 and S8 show ORTEP plots of the crystal structures of $[CrEuCr(\mathbf{L2})_3](CF_3SO_3)_9(C_2H_5N)_{30}$ and $[CrYbCr(\mathbf{L2})_3](CF_3SO_3)_9(C_2H_5N)_{30}$, respectively.

(S1) Van der Sluis, P.; Spek, A. L. *Acta Cryst*. **1990**, *A46***,** 194-201.

Table S1 Elemental Analyses for $[ZnLnZn(\mathbf{L2})_3](CF_3SO_3)_7{\cdot}nH_2O$ and $[CrLnCr(\mathbf{L2})_3](CF_3SO_3)_9{\cdot}m$TBAf$\cdot nH_2O$ Complexes (Ln = Nd, Er, Yb; TBAf = $Bu_4NCF_3SO_3$).

Compound	*MM*/ g·mol^{-1}	%C found	%H found	%N found	%C calc	%H calc	%N calc
$[Zn_2Nd(\mathbf{L2})_3](CF_3SO_3)_7{\cdot}6H_2O$	3853.7	49.85	3.53	11.97	49.87	3.68	11.99
$[Zn_2Er(\mathbf{L2})_3](CF_3SO_3)_7{\cdot}9H_2O$	3937.8	48.77	3.45	11.67	48.80	3.76	11.74
$[Zn_2Yb(\mathbf{L2})_3](CF_3SO_3)_7{\cdot}9H_2O$	3929.6	48.88	3.52	11.71	48.90	3.76	11.76
$[Cr_2Nd(\mathbf{L2})_3](CF_3SO_3)_9$ 0.25TBAf$\cdot 2H_2O$	4151.5	48.11	3.79	11.46	48.11	3.44	11.22
$[Cr_2Er(\mathbf{L2})_3](CF_3SO_3)_9$ $\cdot 17H_2O$	4352.4	44.70	3.56	10.48	44.71	3.78	10.62
$[Cr_2Yb(\mathbf{L2})_3](CF_3SO_3)_9$ 0.5TBAf$\cdot 3H_2O$	4284.0	47.67	3.92	11.19	47.67	3.57	10.94

Table S2 Molecular Peaks and their Triflate Adducts Observed by ESI-MS (positive mode) for $[ZnLnZn(\mathbf{L2})_3](CF_3SO_3)_7 \cdot nH_2O$ and $[CrLnCr(\mathbf{L2})_3](CF_3SO_3)_9 \cdot m\text{TBAF} \cdot nH_2O$ (Ln = Nd, Er, Yb, acetonitrile, $3\text{-}5 \cdot 10^{-4}$ M).

Cationic species	Ln = Nd	Ln = Er	Ln = Yb
	m/*z*	*m*/*z*	*m*/*z*
$[Zn_2Ln(\mathbf{L2})_3(CF_3SO_3)]^{6+}$	-	479.9	480.9
$[Zn_2Ln(\mathbf{L2})_3(CF_3SO_3)_2]^{5+}$	-	605.4	606.6
$[Zn_2Ln(\mathbf{L2})_3(CF_3SO_3)_3]^{4+}$	-	794.1	795.2
$[Zn_2Ln(\mathbf{L2})_3(CF_3SO_3)_4]^{3+}$	1099.9	1107.7	1110.6
$[Cr_2Ln(\mathbf{L2})_3(CF_3SO_3)_2]^{7+}$	425.3	428.7	429.2
$[Cr_2Ln(\mathbf{L2})_3(CF_3SO_3)_3]^{6+}$	521.1	524.9	526.0
$[Cr_2Ln(\mathbf{L2})_3(CF_3SO_3)_4]^{5+}$	654.9	659.5	660.8
$[Cr_2Ln(\mathbf{L2})_3(CF_3SO_3)_5]^{4+}$	856.1	861.7	863.1
$[Cr_2Ln(\mathbf{L2})_3(CF_3SO_3)_6]^{3+}$	1190.6	1198.5	1200.6
$[Cr_2Ln(\mathbf{L2})_3(CF_3SO_3)_7]^{2+}$	1860.4	1872.0	1875.3

Table S3 ^{1}H NMR Chemical Shifts (δ/ppm with Respect to TMS)) for **L2** and $[ZnLnZn(\mathbf{L2})_3]^{7+}$ (Ln = Nd, Yb, Er; CD_3CN, 293 K).[a]

	L2	$[Zn_2Nd(\mathbf{L2})_3]^{7+}$	$[Zn_2Yb(\mathbf{L2})_3]^{7+}$	$[Zn_2Er(\mathbf{L2})_3]^{7+}$
H1	8.48	7.44	8.95	[b]
H2	7.61	7.51	8.43	[b]
H3	8.19	7.69	9.04	[b]
H4	7.32	6.67	7.12	[b]
H5	7.21	6.78	6.37	[b]
H6	7.67	3.05	9.02	[b]
H7,7’	4.25	3.07, 3.19	4.42, 3.30	7.28, 7.46
H8	7.63	-0.07	17.46	10.43
H9	7.19	7.14	8.33	[b]
H10	7.30	8.69	7.75	[b]
H11	8.33	10.81	4.61	2.67
H12	7.98	9.98	5.48	3.20
H13	2.37	1.87	2.70	[b]
H14	4.19	3.60	4.98	[b]
H15	4.17	5.28	1.36	[b]

[a] Numbering scheme is given in Fig. S5. [b] Incomplete assignments due to strong paramagnetic effects (Fig. S5c).[23]

Table S4 Selected Characteristic Luminescence Lifetimes for Ligand-Centred and Metal-Centred Excited States in **L2**, $[ZnLnZn(\mathbf{L2})_3]^{7+}$ and $[CrLnCr(\mathbf{L2})_3]^{9+}$ (Ln = Nd, Gd Yb, Er) in the Solid State Under Various Conditions

Compounds	T / K	$\tilde{\nu}_{exc}$ /cm^{-1}	$\tilde{\nu}_{an}$ / cm^{-1}	τ / μs	Assignment
L2	77	31505	22780	-	$L(^1\pi^*\rightarrow\pi)$
$[ZnGdZn(\mathbf{L2})_3]^{7+}$	77	24690	22520	-	$L(^1\pi^*\rightarrow\pi)$
			20100	$2.45(9)\cdot10^3$	$L(^3\pi^*\rightarrow\pi)$ (tridentate)
$[CrGdGd(\mathbf{L2})_3]^{7+}$	10	31250	24510	$5.19(1)\cdot10^3$	$L(^3\pi^*\rightarrow\pi)$ (didentate)
			21050	$1.58(1)\cdot10^3$	$L(^3\pi^*\rightarrow\pi)$ (tridentate)
		21468	13245	$2.27(1)\cdot10^3$	$Cr(^2E\rightarrow{}^4A_2)$
	295	21468	133316	31(1)	$Cr(^2E\rightarrow{}^4A_2)$
$[ZnNdZn(\mathbf{L2})_3]^{7+}$	40	24390	11494	1.67(1)	$Nd(^4F_{3/2}\rightarrow{}^4I_{9/2})$
		24390	11364	1.62(1)	$Nd(^4F_{3/2}\rightarrow{}^4I_{9/2})$
		24390	9328	1.56(1)	$Nd(^4F_{3/2}\rightarrow{}^4I_{11/2})$
		24390	9302	1.55(1)	$Nd(^4F_{3/2}\rightarrow{}^4I_{11/2})$
	295	24390	9346	1.42(1)	$Nd(^4F_{3/2}\rightarrow{}^4I_{11/2})$
		24390	9328	1.40(1)	$Nd(^4F_{3/2}\rightarrow{}^4I_{11/2})$
		24390	11494	1.57(1)	$Nd(^4F_{3/2}\rightarrow{}^4I_{9/2})$
		24390	11364	1.59(1)	$Nd(^4F_{3/2}\rightarrow{}^4I_{9/2})$
		24390	11236	1.54(1)	$Nd(^4F_{3/2}\rightarrow{}^4I_{9/2})$
$[ZnErZn(\mathbf{L2})_3]^{7+}$	10	28169	20833	1.44(4)	$L(^3\pi^*\rightarrow\pi)$
		28169	18181	2.9(1)	$Er(^4S_{3/2}\rightarrow{}^4I_{15/2})$
		28169	16129	0.52(4)	$Er(^4G_{11/2}\rightarrow{}^4I_{11/2})$
		28169	14286	0.18(1)	$Er(^2H_{9/2}\leftarrow{}^4I_{11/2})$
		21980	6450	4.54(1)	$Er(^4I_{13/2}\rightarrow{}^4I_{15/2})$
$[ZnYbZn(\mathbf{L2})_3]^{7+}$	40	28170	10204	31.0(2)	$Yb(^2F_{5/2}\rightarrow{}^2F_{7/2})$
	295	28170	10309	26.3(2)	$Yb(^2F_{5/2}\rightarrow{}^2F_{7/2})$
		28170	10204	30.1(1)	$Yb(^2F_{5/2}\rightarrow{}^2F_{7/2})$
		28170	10101	26.9(1)	$Yb(^2F_{5/2}\rightarrow{}^2F_{7/2})$
		28170	10000	26.7(1)	$Yb(^2F_{5/2}\rightarrow{}^2F_{7/2})$

Table S4 Continuation

$[CrNdCr(\mathbf{L2})_3]^{9+}$	10	28169	13333	500(20)	$Cr(^2E\rightarrow{}^4A_2)$
		22222	13333	500(20)	$Cr(^2E\rightarrow{}^4A_2)$
		22222	9346)	250(50)	$Nd(^4F_{3/2}\rightarrow{}^4I_{11/2})$
	77	25000	13245	220(20)	$Cr(^2E\rightarrow{}^4A_2)$
	295	28169	13333	30(5)	$Cr(^2E\rightarrow{}^4A_2)$
		25000	13333	30(5)	$Cr(^2E\rightarrow{}^4A_2)$
		22222	13333	30(5)	$Cr(^2E\rightarrow{}^4A_2)$
		28169	9346	4.5(5)	$Nd(^4F_{3/2}\rightarrow{}^4I_{11/2})$
		22222	9346	30(5)	$Nd(^4F_{3/2}\rightarrow{}^4I_{11/2})$
$[CrErCr(\mathbf{L2})_3]^{9+}$	10	28169	13333	1071(50)	$Cr(^2E\rightarrow{}^4A_2)$
		22222	13333	1075(50)	$Cr(^2E\rightarrow{}^4A_2)$
		21980	6450	1080(80)	$Er(^4I_{13/2}\rightarrow{}^4I_{15/2})$
	77	29412	13175)	637(30)	$Cr(^2E\rightarrow{}^4A_2)$
		25000	13175	683(30)	$Cr(^2E\rightarrow{}^4A_2)$
		21739	13175	817(35)	$Cr(^2E\rightarrow{}^4A_2)$
	295	28169	13333	40(5)	$Cr(^2E\rightarrow{}^4A_2)$
		28169	6452	0.34(5)	$Er(^4I_{13/2}\rightarrow{}^4I_{15/2})$
		22222	13333	40(5)	$Cr(^2E\rightarrow{}^4A_2)$
		22222	6452	30(4)	$Er(^4I_{13/2}\rightarrow{}^4I_{15/2})$
$[CrYbCr(\mathbf{L2})_3]^{9+}$	10	28169	13333	$1.326(6)\cdot10^3$	$Cr(^2E\rightarrow{}^4A_2)$
		22222	13333	$1.450(1)\cdot10^3$	$Cr(^2E\rightarrow{}^4A_2)$
		28169	10204	26.7(13)	$Yb(^2F_{5/2}\rightarrow{}^2F_{7/2})$
		22222	10204	$1.306(15)\cdot10^3$	$Yb(^2F_{5/2}\rightarrow{}^2F_{7/2})$
	77	25000	13210	510(40)	$Cr\ (^2E\rightarrow{}^4A_2)$
	295	28169	13333	22.1(2)	$Cr(^2E\rightarrow{}^4A_2)$
		25000	13333	30(5)	$Cr(^2E\rightarrow{}^4A_2)$
		22222	13333	48(1)	$Cr(^2E\rightarrow{}^4A_2)$
		28169	10204	27.8(2)	$Yb(^2F_{5/2}\rightarrow{}^2F_{7/2})$
		22222	10204	32.3(2)	$Yb(^2F_{5/2}\rightarrow{}^2F_{7/2})$

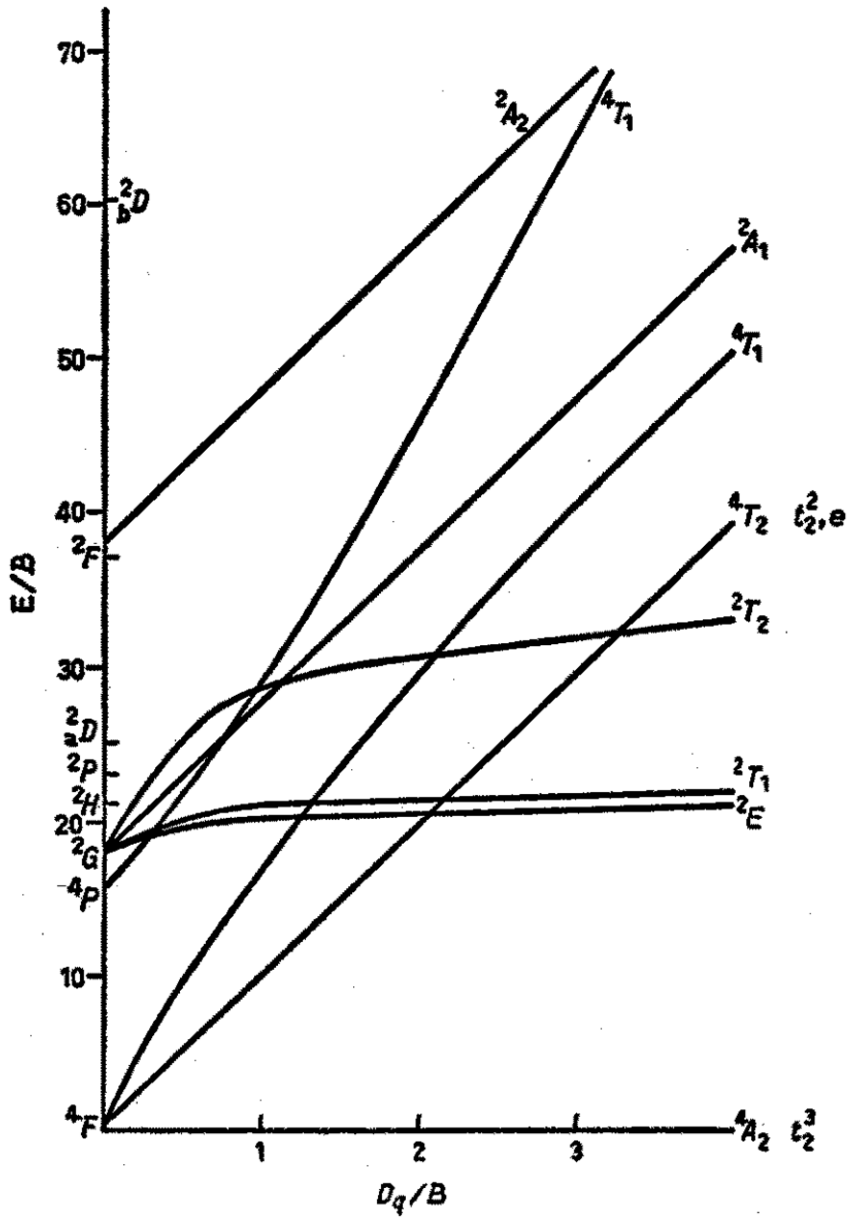

Figure S1 Energy level diagram (Tanabe-Sugano) for d^3 ion in an octahedral field ($C = 4.5\ B$).[14a]

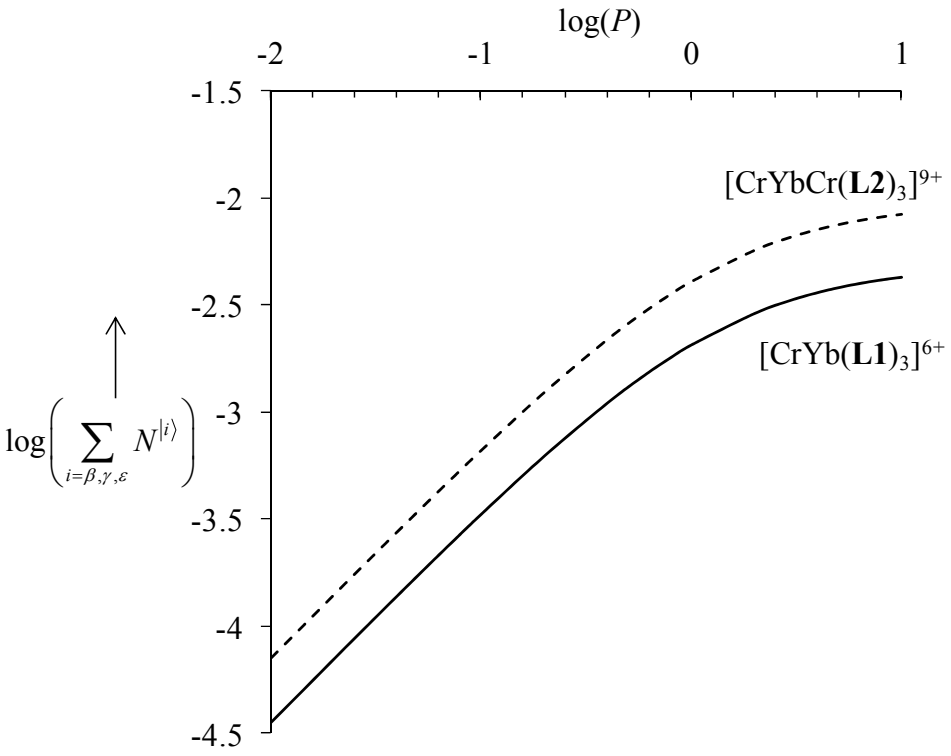

Figure S2 Computed linear dependence of Yb-centered emission intensity with respect to incident pump power (in W/mm^2) of the Cr-centered transition in $[CrYb(\mathbf{L1})_3]^{6+}$ (full trace),[16] and related dependence for $[CrYbCr(\mathbf{L2})_3]^{9+}$ (dashed trace) predicted by using the same rate constants ($W_{Cr\rightarrow Yb}^{CrYbCr} \equiv W_{Cr\rightarrow Yb}^{CrYb} = W_{Cr\rightarrow Yb} = 240\ s^{-1}$, $k_{Cr}^{CrGdCr} \equiv k_{Cr}^{CrGd} = 270\ s^{-1}$ and $k_{Yb}^{ZnYbZn} \equiv k_{Yb}^{ZnYb} = 5\cdot10^4\ s^{-1}$).

a)

$$\boldsymbol{M} = \begin{pmatrix} -2k_{\mathrm{Cr}}^{\mathrm{exc}} & k_{\mathrm{Cr}}^{\mathrm{CrGdCr}} & k_{\mathrm{Yb}}^{\mathrm{ZnYbZn}} & 0 & 0 & 0 \\ 2k_{\mathrm{Cr}}^{\mathrm{exc}} & -\left(k_{\mathrm{Cr}}^{\mathrm{CrGdCr}} + k_{\mathrm{Cr}}^{\mathrm{exc}} + W_{\mathrm{Cr}\rightarrow\mathrm{Yb}}\right) & 0 & k_{\mathrm{Yb}}^{\mathrm{ZnYbZn}} & 2k_{\mathrm{Cr}}^{\mathrm{CrGdCr}} & 0 \\ 0 & W_{\mathrm{Cr}\rightarrow\mathrm{Yb}} & -\left(2k_{\mathrm{Cr}}^{\mathrm{exc}} + k_{\mathrm{Yb}}^{\mathrm{ZnYbZn}}\right) & k_{\mathrm{Cr}}^{\mathrm{CrGdCr}} & 0 & 0 \\ 0 & 0 & 2k_{\mathrm{Cr}}^{\mathrm{exc}} & -\left(k_{\mathrm{Cr}}^{\mathrm{exc}} + k_{\mathrm{Cr}}^{\mathrm{CrGdCr}} + k_{\mathrm{Yb}}^{\mathrm{ZnYbZn}}\right) & 2W_{\mathrm{Cr}\rightarrow\mathrm{Yb}} & 2k_{\mathrm{Cr}}^{\mathrm{CrGdCr}} \\ 0 & k_{\mathrm{Cr}}^{\mathrm{exc}} & 0 & 0 & -\left(2k_{\mathrm{Cr}}^{\mathrm{CrGdCr}} + 2W_{\mathrm{Cr}\rightarrow\mathrm{Yb}}\right) & k_{\mathrm{Yb}}^{\mathrm{ZnYbZn}} \\ 0 & 0 & 0 & k_{\mathrm{Cr}}^{\mathrm{exc}} & 0 & -\left(2k_{\mathrm{Cr}}^{\mathrm{CrGdCr}} + k_{\mathrm{Yb}}^{\mathrm{ZnYbZn}}\right) \end{pmatrix}$$

b)

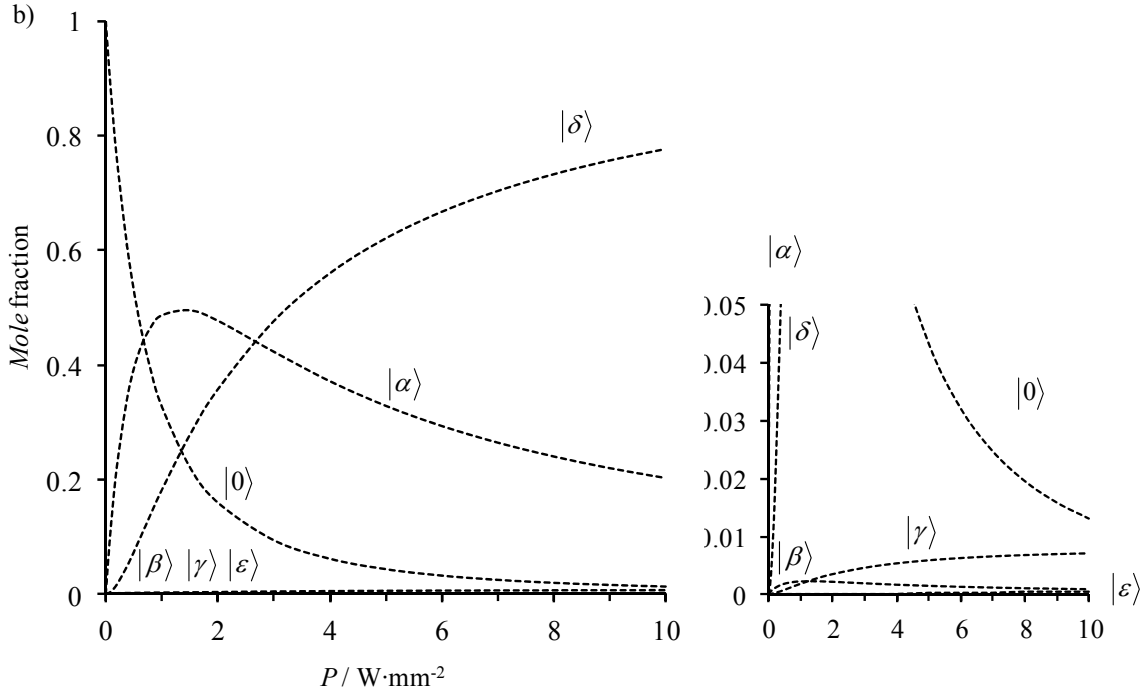

Figure S3 a) Kinetic matrix for the Jablonski diagram shown in Fig. 3b and b) predicted steady-state population densities for the various levels (the 0-0.05 population density range is highlighted on the right) for $[CrYbCr(\mathbf{L2})_3]^{9+}$ upon irradiation of the Cr-centered transitions ($k_{\mathrm{Cr}}^{\mathrm{CrGdCr}} \equiv k_{\mathrm{Cr}}^{\mathrm{CrGd}} = 270\ \mathrm{s}^{-1}$, $k_{\mathrm{Yb}}^{\mathrm{ZnYbZn}} \equiv k_{\mathrm{Yb}}^{\mathrm{ZnYb}} = 5\cdot10^{4}\ \mathrm{s}^{-1}$, $W_{\mathrm{Cr}\rightarrow\mathrm{Yb}}^{\mathrm{CrYbCr}} \equiv W_{\mathrm{Cr}\rightarrow\mathrm{Yb}}^{\mathrm{CrYb}} = W_{\mathrm{Cr}\rightarrow\mathrm{Yb}} = 240\ \mathrm{s}^{-1}$) with increasing incident pump power P.[18b]

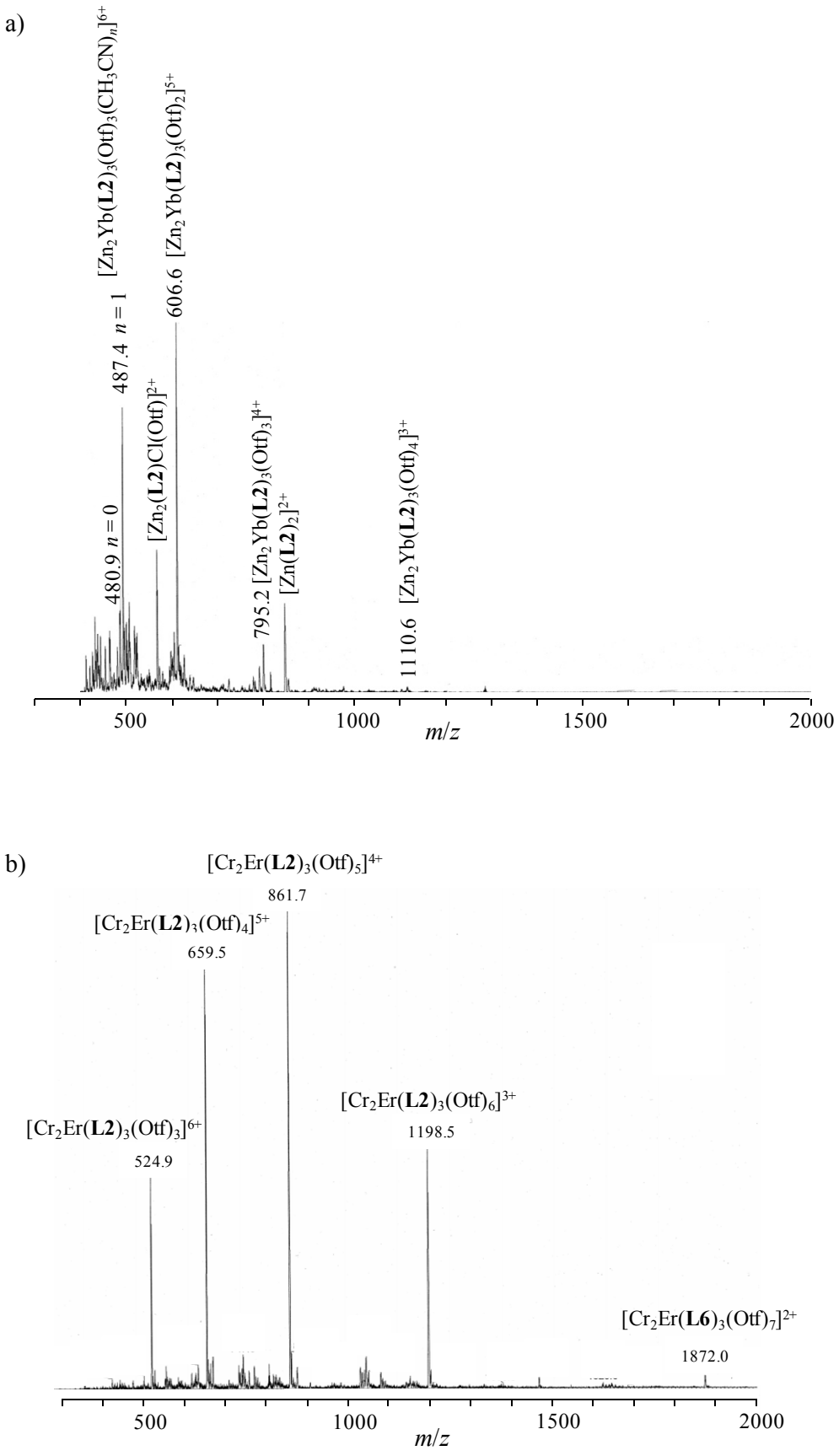

Figure S4 ESI-MS spectra of a) $[ZnYbZn(\mathbf{L2})_3](CF_3SO_3)_7$ and b) $[CrErCr(\mathbf{L2})_3](CF_3SO_3)_9$ ($3\text{-}5\cdot10^{-4}$ M, CH_3CN, 298 K, $Otf^- = CF_3SO_3^-$).

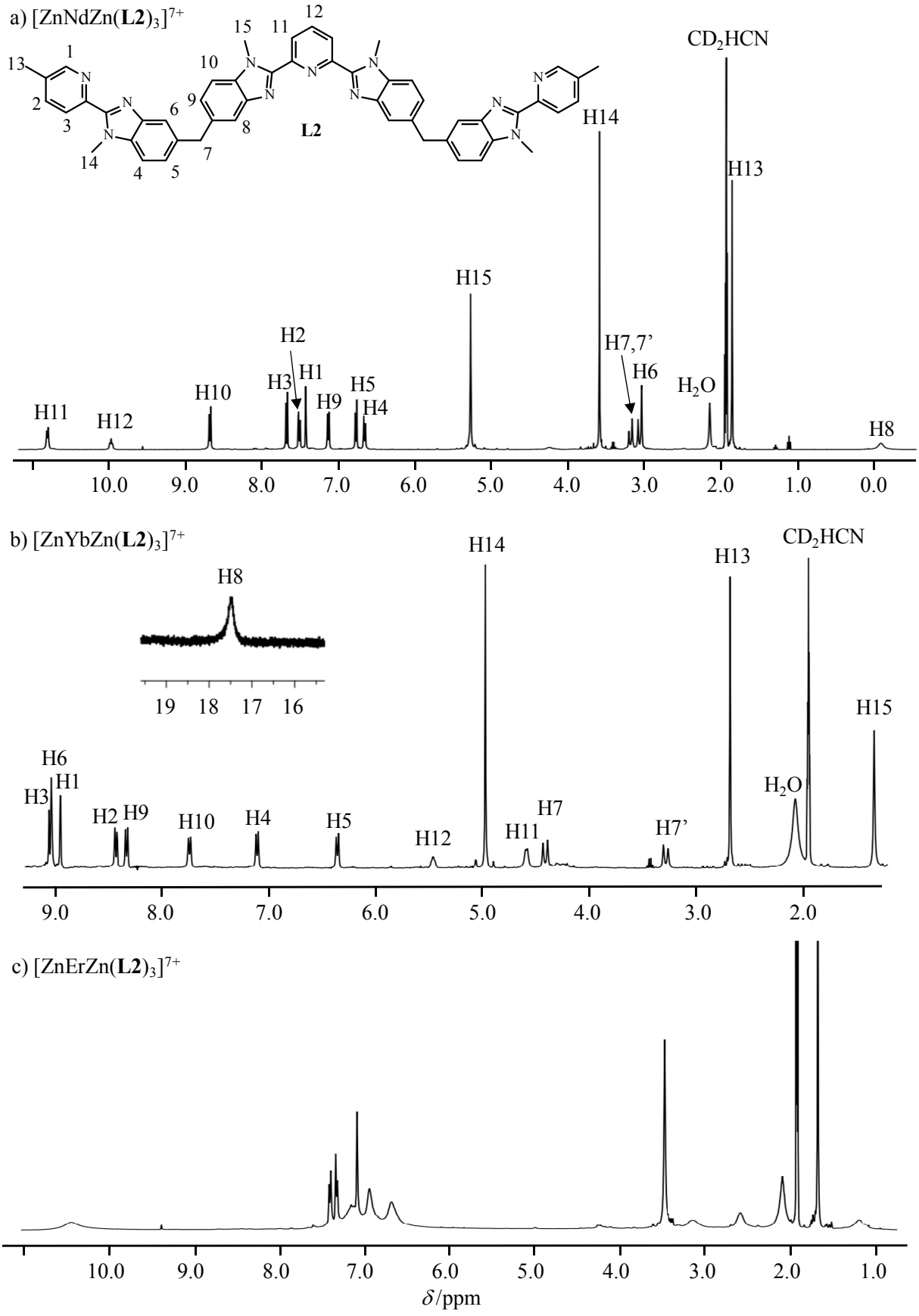

Figure S5 ^{1}H NMR spectra of a) $[ZnNdZn(\mathbf{L2})_3]^{7+}$, b) $[ZnYbZn(\mathbf{L2})_3]^{7+}$and c) $[ZnErZn(\mathbf{L2})_3]^{7+}$ (CD_3CN, 293 K).

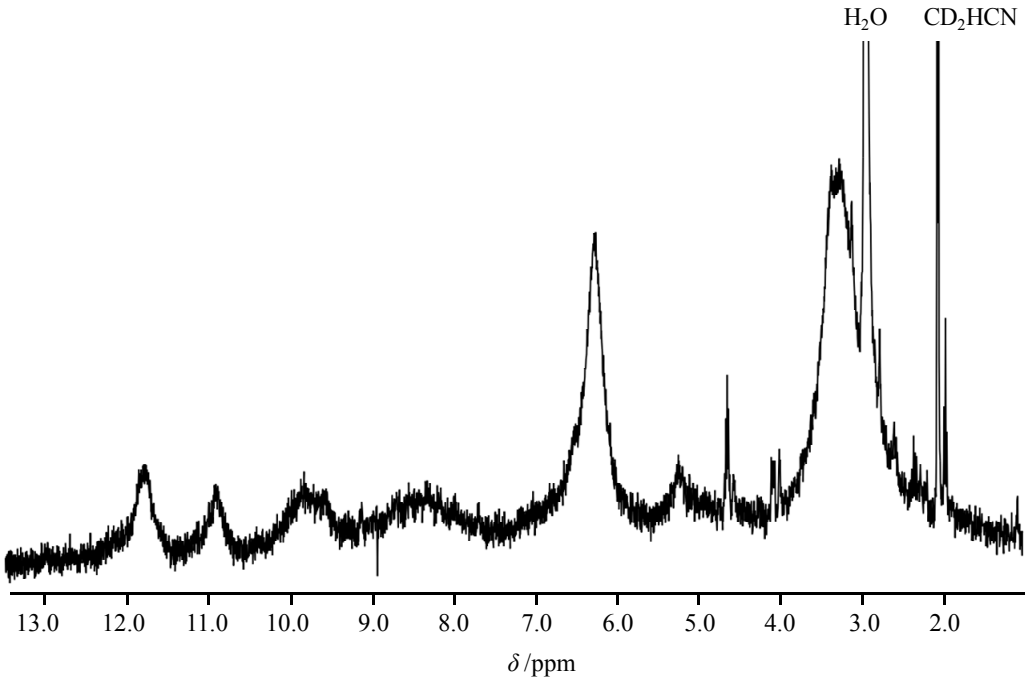

Figure S6 Part of the ^{1}H NMR spectrum of $[CrNdCr(\mathbf{L2})_3]^{9+}$ (CD_3CN, 293 K).

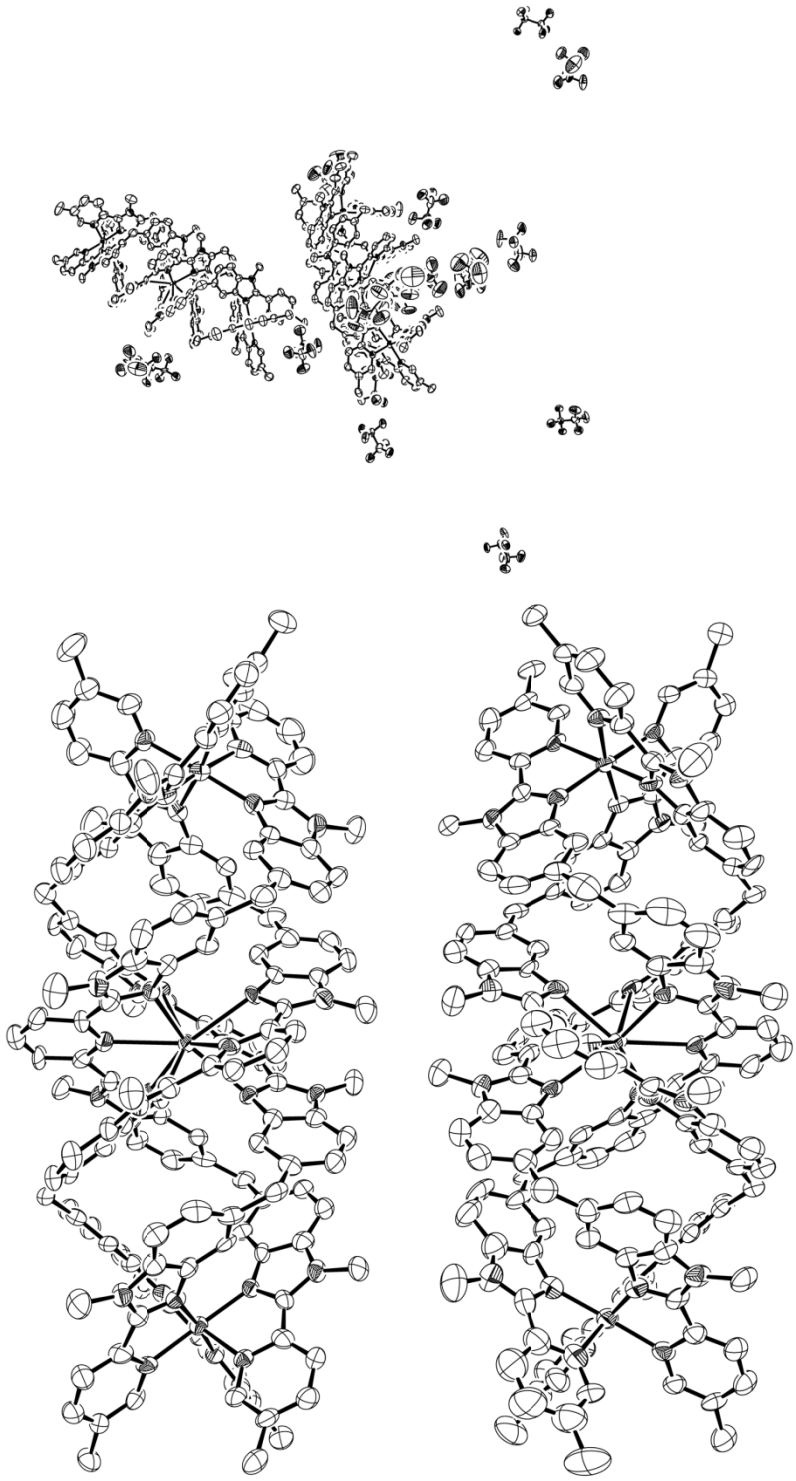

Figure S7 Perspective ORTEP views of a) the assymetric unit and b) the molecular structures of the two triple-helical $[CrEuCr(\mathbf{L2})_3]^{9+}$ cations along their pseudo-threefold axes in the asymmetric unit of $[CrEuCr(\mathbf{L2})_3]_2(CF_3SO_3)_{18}(C_3H_5N)_{30}$. Ellipsoids are represented at the 50% probability level. Hydrogen atoms are omitted for clarity.

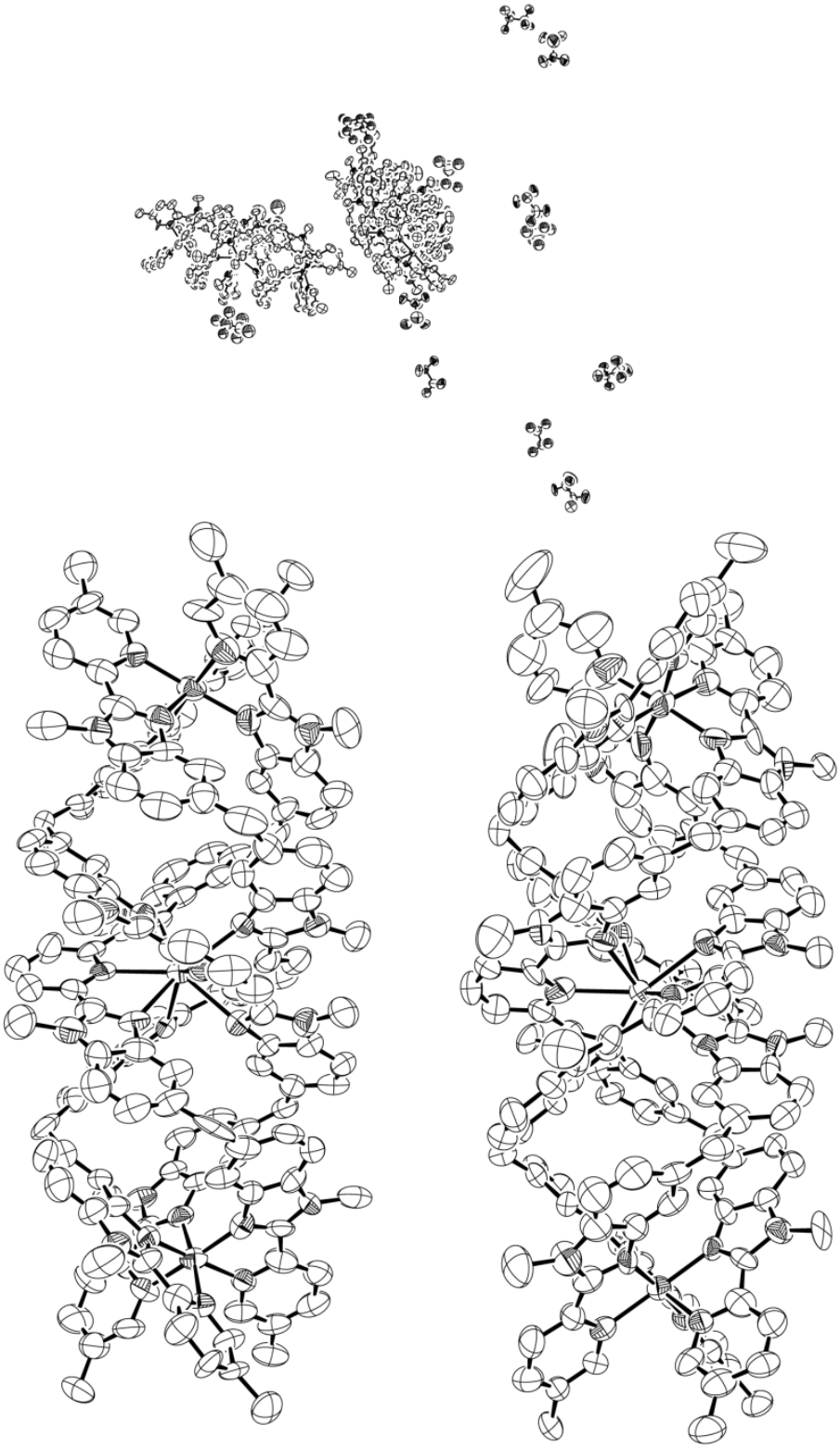

Figure S8 Perspective ORTEP views of a) the assymetric unit and b) the molecular structures of the two triple-helical $[CrYbCr(\mathbf{L2})_3]^{9+}$ cations along their pseudo-threefold axes in the asymmetric unit of $[CrYbCr(\mathbf{L2})_3]_2(CF_3SO_3)_{18}(C_3H_5N)_{30}$. Ellipsoids are represented at the 50% probability level. Hydrogen atoms are omitted for clarity.

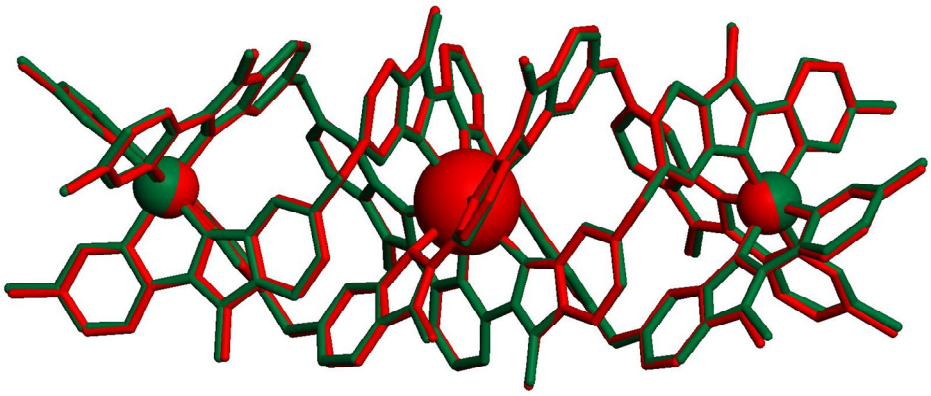

Figure S9 Superimposition of the molecular structures of $[CrEuCr(\mathbf{L2})_3]^{9+}$ (red) and $[CrYbCr(\mathbf{L2})_3]^{9+}$ (green) in the crystal structures of $[CrLnCr(\mathbf{L2})_3](CF_3SO_3)_9(C_3H_5N)_{30}$. Hydrogen atoms have been omitted for clarity

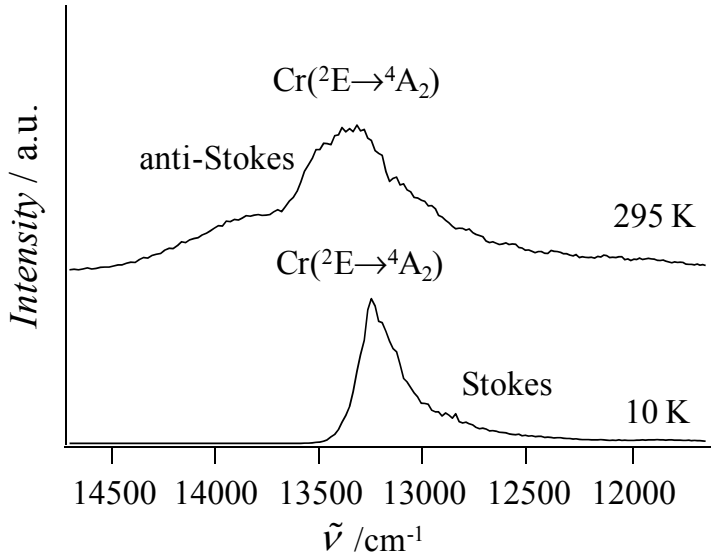

Figure S10 Emission spectra for $[CrGdCr(\mathbf{L2})_3](CF_3SO_3)_9$ at 10 K and 295 K ($\tilde{\nu}_{exc}$ = 28170 cm^{-1}).

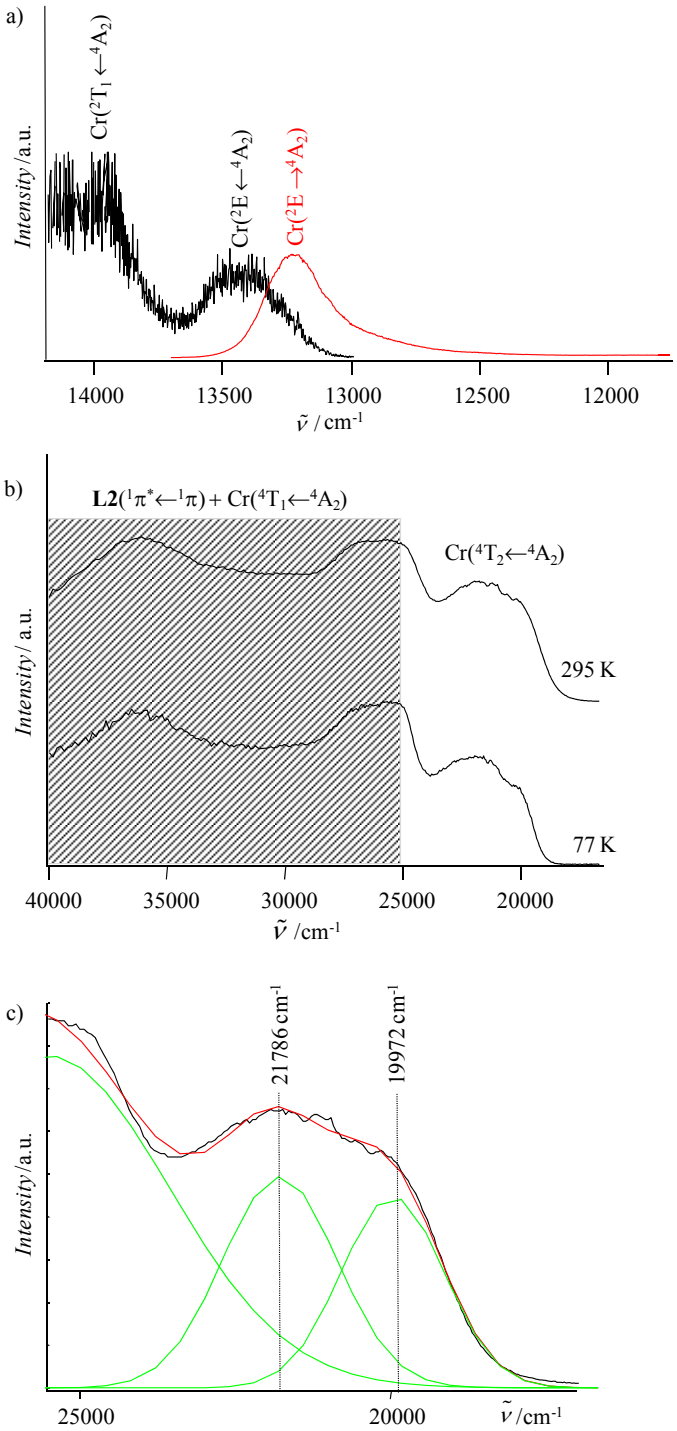

Figure S11 Sensitization of the Cr(^{2}E→^{4}A$_2$) NIR emission in [CrGdCr(**L1**)$_3$](CF$_3$SO$_3$)$_9$. A) Low-energy excitation spectrum (black trace, $\tilde{\nu}_{an}$ = 12821 cm^{-1}, 10 K) and emission spectrum (red trace, $\tilde{\nu}_{exc}$ = 13888 cm^{-1}, 10 K). B) High-energy excitation spectrum recorded upon monitoring the Cr(^{2}E→^{4}A$_2$) emission (solid state). The shaded areas correspond to the region of high absorption coefficients of the ligand-centred $^1\pi^*\leftarrow{}^1\pi$ transitions leading to artefacts due to the lack of penetration of the incident light. C) Deconvolution of the Cr(^{4}T$_2$←^{4}A$_2$) transition (O_h symmetry) into its A+E components in D_3-symmetry in [CrGdCr(**L1**)$_3$](CF$_3$SO$_3$)$_9$ (solid state, 295 K).

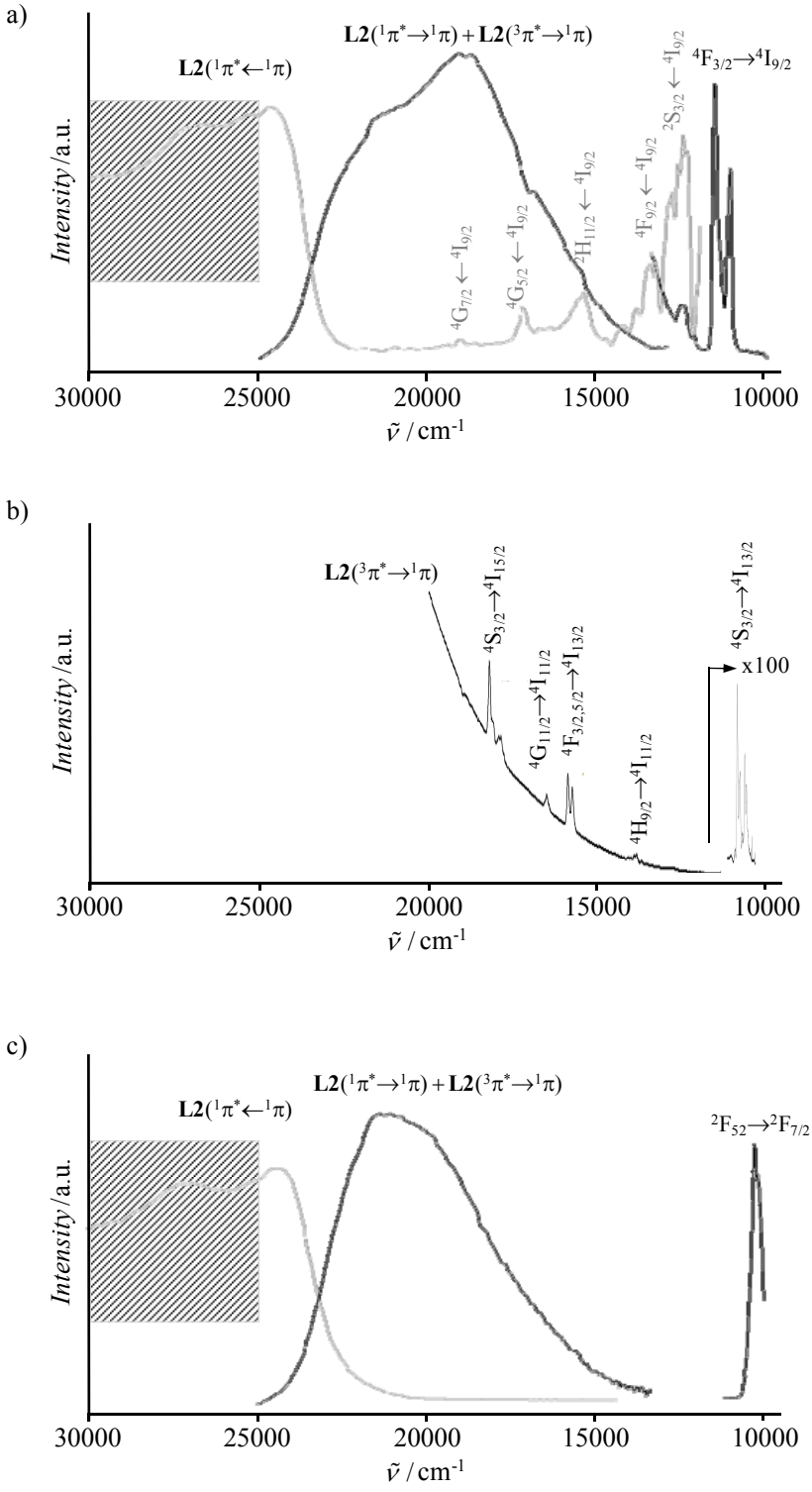

Figure S12 Solid state excitation (grey traces) and emission (black traces, $\tilde{\nu}_{exc}$ = 28170 cm^{-1}) spectra recorded for a) [ZnNdZn(**L2**)$_3$](CF$_3$SO$_3$)$_7$ ($\tilde{\nu}_{an}\left[\mathrm{Nd}\left({}^4\mathrm{F}_{3/2} \rightarrow {}^4\mathrm{I}_{3/2}\right)\right]$, 295 K), b) b) [ZnErZn(**L2**)$_3$](CF$_3$SO$_3$)$_7$ (10 K) and c) [ZnYbZn(**L2**)$_3$](CF$_3$SO$_3$)$_7$ ($\tilde{\nu}_{an}\left[\mathrm{Yb}\left({}^2\mathrm{F}_{5/2} \rightarrow {}^2\mathrm{F}_{7/2}\right)\right]$, 295 K). The shaded areas correspond to the region of high absorption coefficients of the ligand-centred $^1\pi^*\leftarrow{}^1\pi$ transitions leading to artefacts due to the lack of penetration of the incident light.

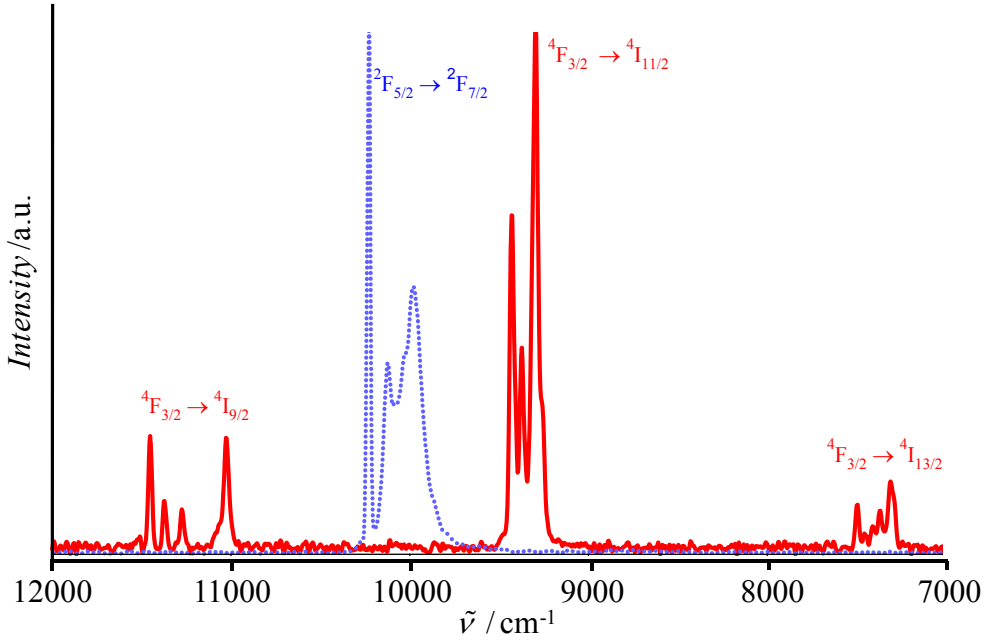

Figure S13 High-resolution solid state NIR emission spectra ($\tilde{\nu}_{exc}$ = 24690 cm^{-1}, 10 K) recorded for [ZnNdZn(**L2**)$_3$](CF$_3$SO$_3$)$_7$ (red trace) and [ZnYbZn(**L2**)$_3$](CF$_3$SO$_3$)$_7$ (blue trace).

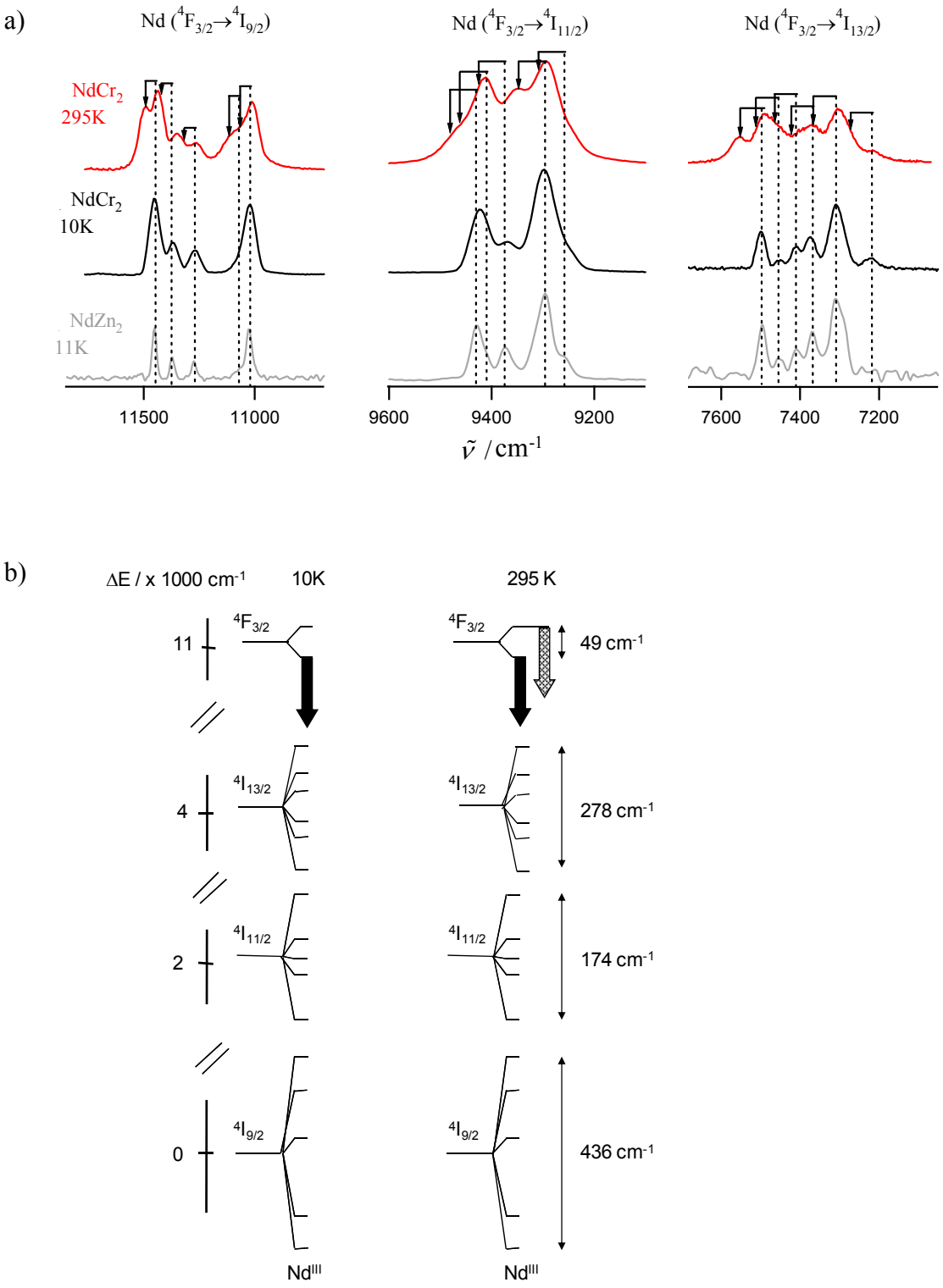

Figure S14 a) High-resolution solid state emission spectra of [ZnNdZn(**L2**)$_3$](CF$_3$SO$_3$)$_7$ and [CrNdCr(**L2**)$_3$](CF$_3$SO$_3$)$_9$ showing isostructurality around Nd(III) and b) associated crystal-field splittings.

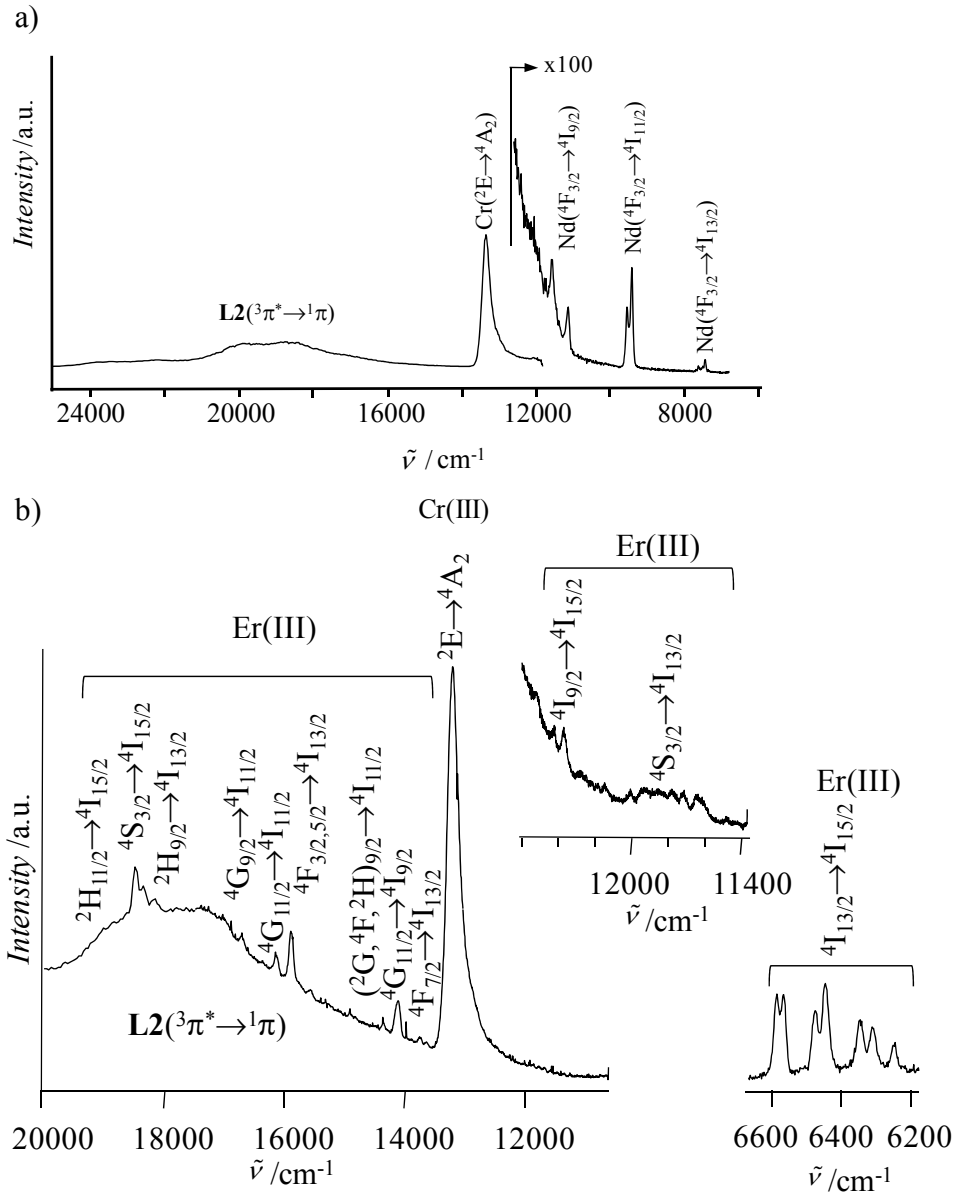

Figure S15 Emission spectra recorded for a) $[CrNdCr(\mathbf{L2})_3](CF_3SO_3)_9$ and b) $[CrErCr(\mathbf{L2})_3](CF_3SO_3)_9$ upon ligand-centered excitation ($\tilde{\nu}_{exc}$ = 37037 cm^{-1}, solid state, 77 K).

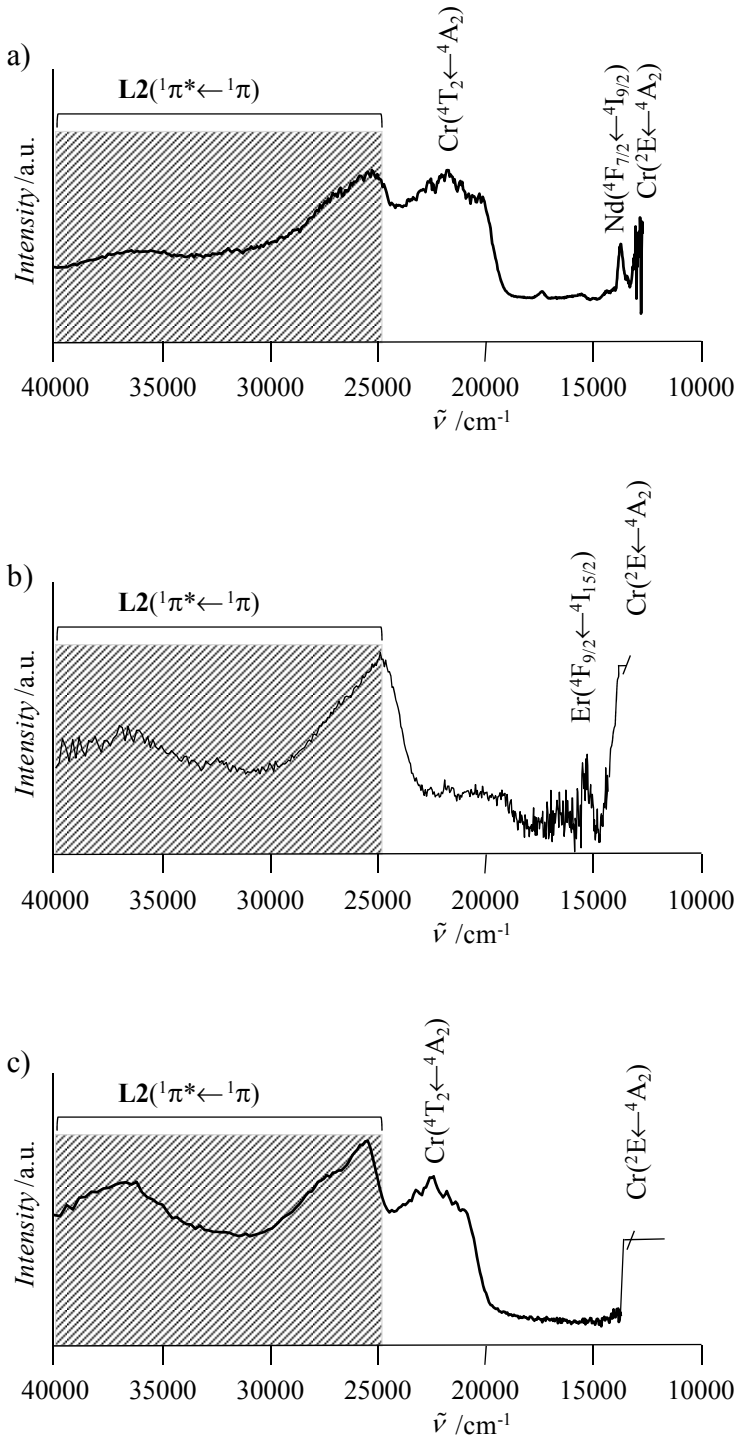

Figure S16 Solid state excitation spectra recorded at 77 K for a) $[CrNdCr(\mathbf{L1})_3](CF_3SO_3)_9$. ($\tilde{\nu}_{an}\left({}^4F_{3/2} \rightarrow {}^4I_{11/2}\right)$ = 9314 cm^{-1}), b) $[CrErCr(\mathbf{L1})_3](CF_3SO_3)_9$. ($\tilde{\nu}_{an}\left({}^4I_{13/2} \rightarrow {}^4I_{15/2}\right)$ = 6569 cm^{-1}) and c) $[CrYbCr(\mathbf{L1})_3](CF_3SO_3)_9$. ($\tilde{\nu}_{an}\left({}^2F_{5/2} \rightarrow {}^2F_{7/2}\right)$ = 10294 cm^{-1}. The shaded areas correspond to the region of high absorption coefficients of the ligand-centred $^1\pi^*\leftarrow{}^1\pi$ transitions leading to artefacts due to the lack of penetration of the incident light.

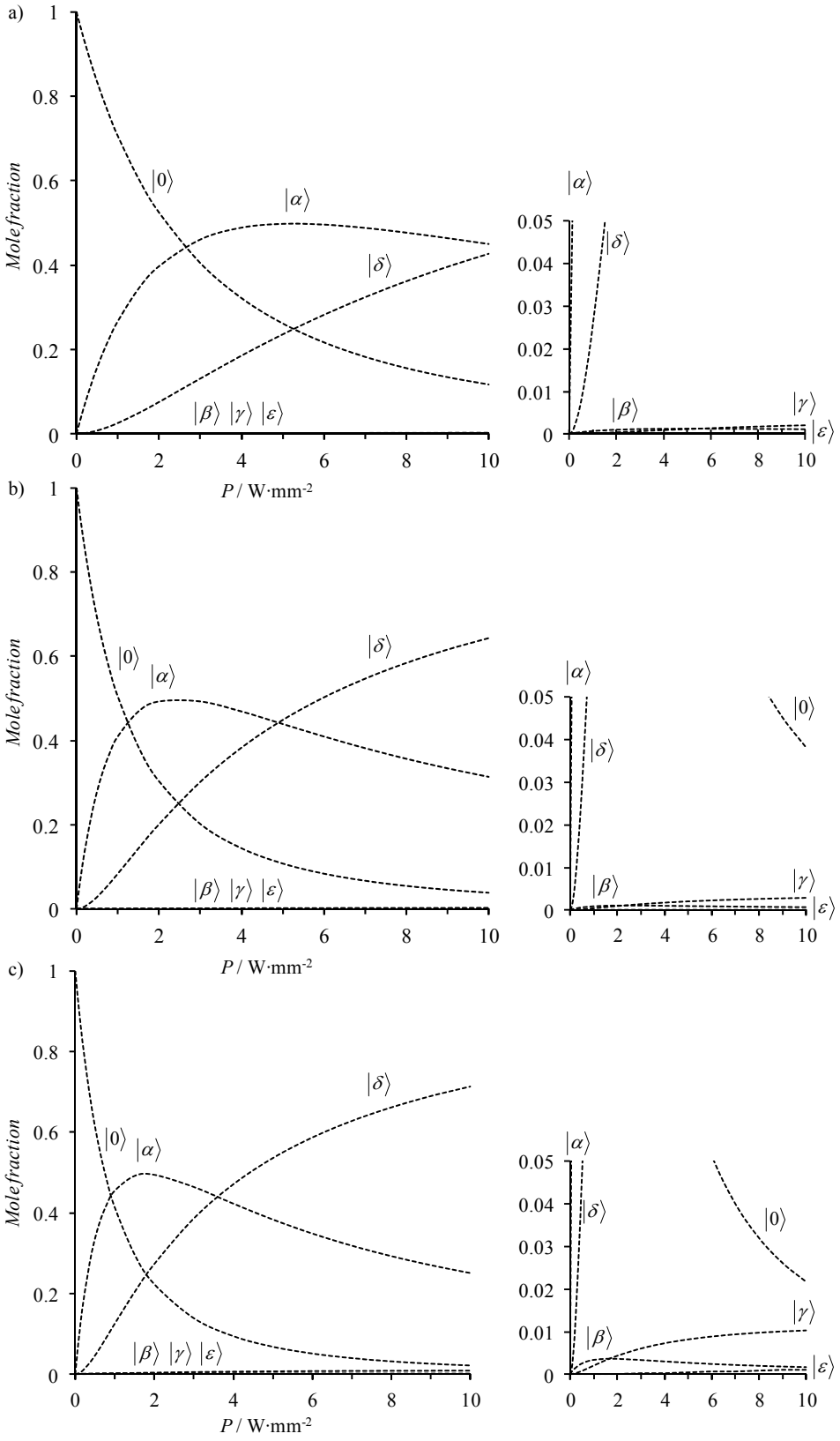

Figure S17 Computed steady-state population densities for the various levels (the 0-0.05 population density range is highlighted on the right) for a) $[CrNdCr(\mathbf{L2})_3]^{9+}$, b) $[CrErCr(\mathbf{L2})_3]^{9+}$ and c) $[CrYbCr(\mathbf{L2})_3]^{9+}$ upon irradiation of the Cr-centered transitions with increasing incident pump power *P* (pertinent rate constants are collected in Table 1).

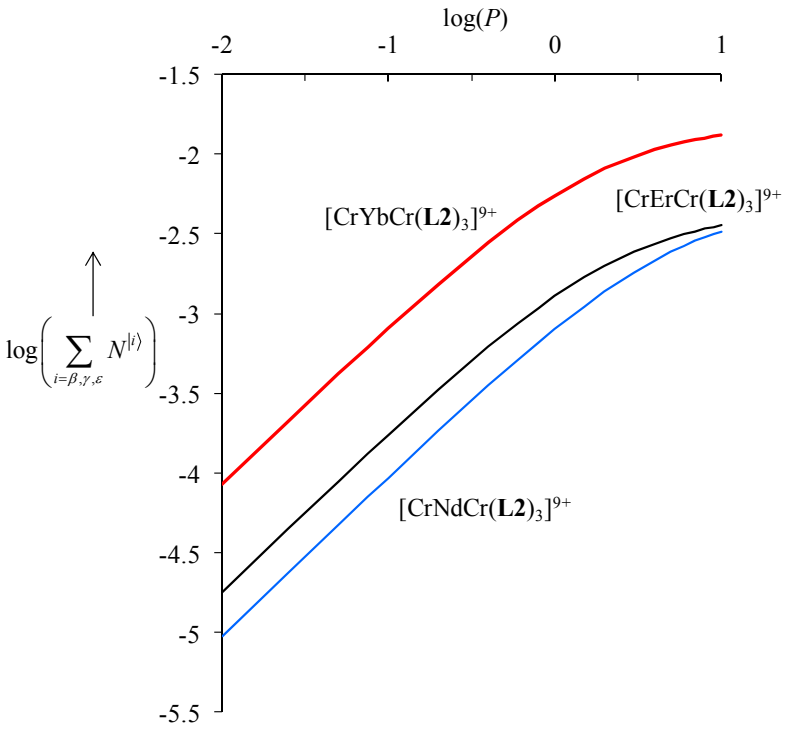

Figure S18 Computed linear dependences of Ln-centered emission intensity with respect to incident pump power (in W/mm^2) of the Cr-centered transitions in [CrNdCr(**L2**)$_3$]$^{9+}$ (blue trace), [CrErCr(**L2**)$_3$]$^{9+}$ (black trace) and [CrYbCr(**L2**)$_3$]$^{9+}$ (red trace).

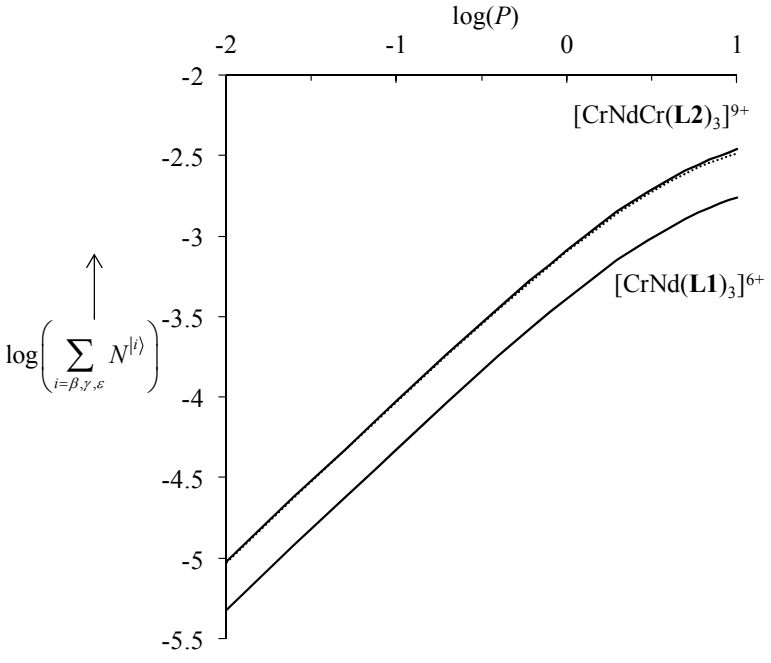

Figure S19 Computed linear dependences of Nd-centered emission intensity with respect to incident pump power (in W/mm^2) of the Cr-centered transition in [CrNd(**L1**)$_3$]$^{6+}$ and [CrNdCr(**L2**)$_3$]$^{9+}$ (full traces, solid state, 10K). The statistical behavior (f_{gain} = 2.0) predicted for [CrNdCr(**L2**)$_3$]$^{9+}$ by using the rate constants of [CrNd(**L1**)$_3$]$^{6+}$ is shown as a dotted trace.

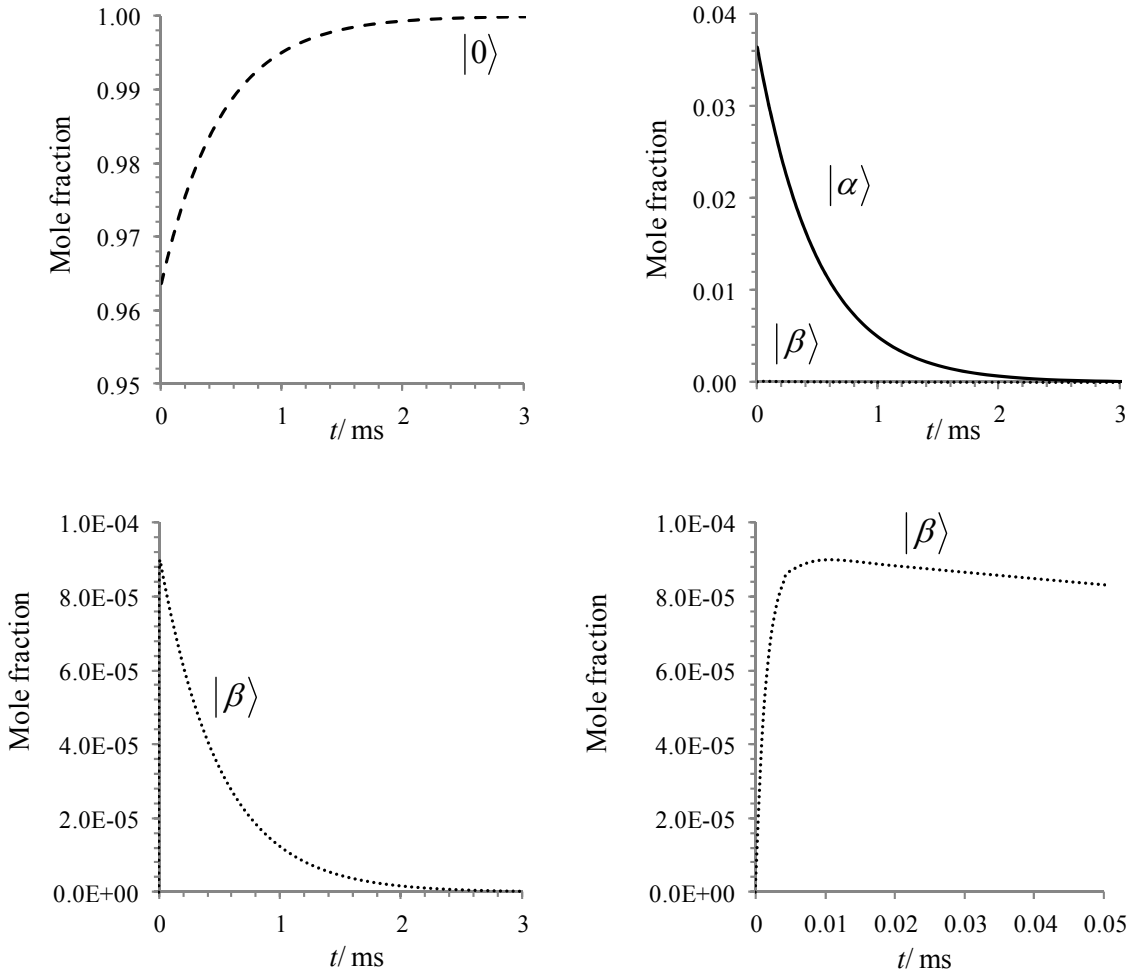

Figure S20 Computed time evolution of the population densities of the ground state CrNdCr ($|0\rangle$, dashed trace, eq. 8), and of the lowest excited states Cr*NdCr ($|\alpha\rangle$, full trace, eq. 9) and CrNd*Cr ($|\beta\rangle$, dotted trace, eq. 10) in $[CrNdCr(\mathbf{L2})_3]^{9+}$ after 500 μJ/mm^2 pulse of 10 ns in the Cr-centered transition (solid state, 10K).

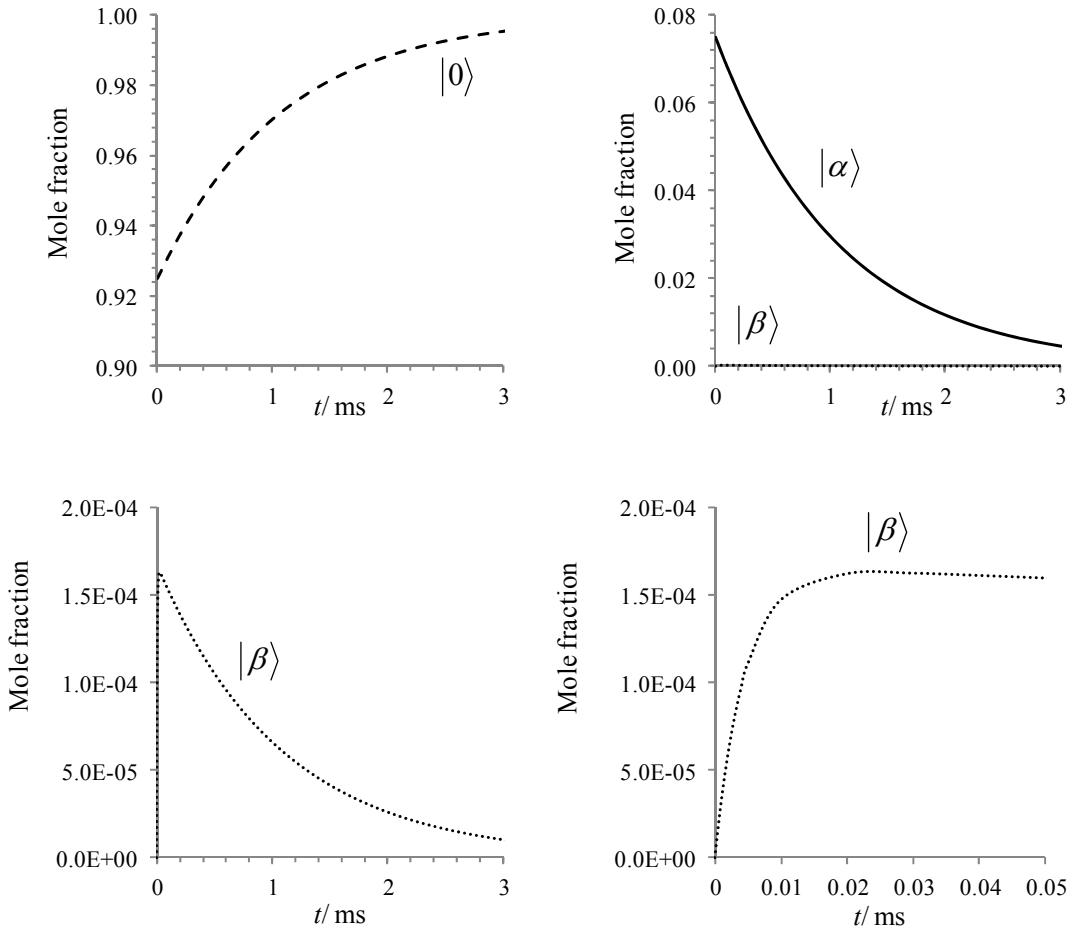

Figure S21 Computed time evolution of the population densities of the ground state CrErCr ($|0\rangle$, dashed trace, eq. 8), and of the lowest excited states Cr*ErCr ($|\alpha\rangle$, full trace, eq. 9) and CrEr*Cr ($|\beta\rangle$, dotted trace, eq. 10) in $[CrErCr(\mathbf{L2})_3]^{9+}$ after a 500 μJ/mm^2 pulse of 10 ns in the Cr-centered transition (solid state, 10K).

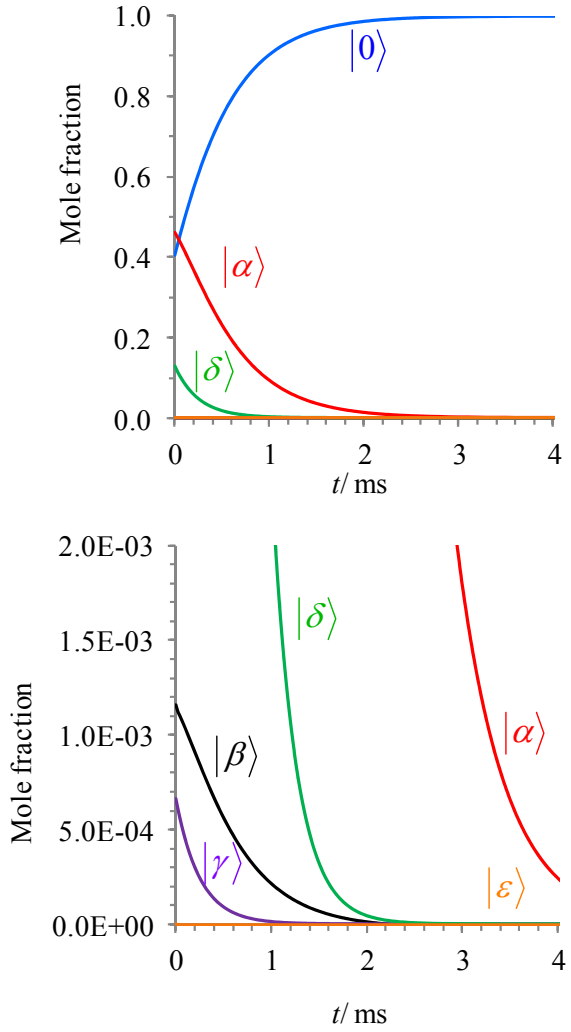

Figure S22 Time evolution of the population densities for the ground state CrNdCr ($|0\rangle$, blue trace) and of the excited states Cr*NdCr ($|\alpha\rangle$, red trace), CrNd*Cr ($|\beta\rangle$, black trace), Cr*Nd*Cr ($|\gamma\rangle$, violet trace), Cr*NdCr* ($|\delta\rangle$, green trace) and Cr*Nd*Cr* ($|\varepsilon\rangle$, orange trace) in $[CrNdCr(\mathbf{L2})_3]^{9+}$ following a 3 W/mm^2 presaturation (solid state, 10K, eq S13).

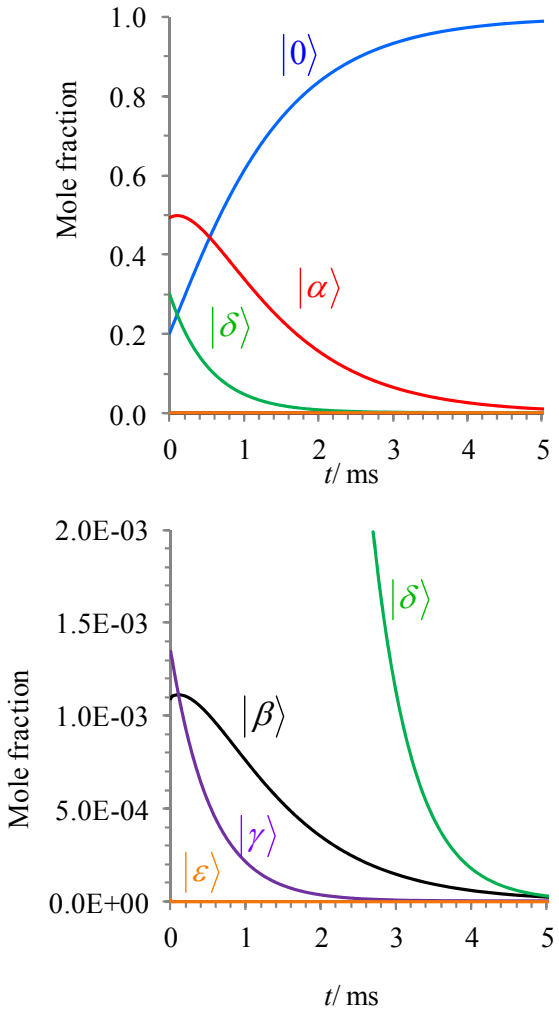

Figure S23 Time evolution of the population densities for the ground state CrErCr ($|0\rangle$, blue trace) and of the excited states Cr*ErCr ($|\alpha\rangle$, red trace), CrEr*Cr ($|\beta\rangle$, black trace), Cr*Er*Cr ($|\gamma\rangle$, violet trace), Cr*ErCr* ($|\delta\rangle$, green trace) and Cr*Er*Cr* ($|\varepsilon\rangle$, orange trace) in $[CrErCr(\mathbf{L2})_3]^{9+}$ following a 3 W/mm^2 presaturation (solid state, 10K, eq S13).

Appendix 1. Projection operator solutions of eq. 7

The solution of the matrix differential eq. (7) is[20]

$$\begin{pmatrix} N_t^{|0\rangle} \\ N_t^{|\alpha\rangle} \\ N_t^{|\beta\rangle} \end{pmatrix} = \exp\left\{ \begin{pmatrix} 0 & k_{\mathrm{Cr}}^{\mathrm{CrGdCr}} & k_{\mathrm{Ln}}^{\mathrm{ZnLnZn}} \\ 0 & -\left(k_{\mathrm{Cr}}^{\mathrm{CrGdCr}} + W_{\mathrm{Cr}\to\mathrm{Ln}}\right) & 0 \\ 0 & W_{\mathrm{Cr}\to\mathrm{Ln}} & -k_{\mathrm{Ln}}^{\mathrm{ZnLnZn}} \end{pmatrix} t \right\} \times \begin{pmatrix} N_0^{|0\rangle} \\ N_0^{|\alpha\rangle} \\ 0 \end{pmatrix} \tag{S1}$$

The matrix exponential can be written as a sum of scalar functions by introducing the eigenvalues λ_i and projection operators $\mathbf{P}_i$ [20]

$$\begin{pmatrix} N_t^{|0\rangle} \\ N_t^{|\alpha\rangle} \\ N_t^{|\beta\rangle} \end{pmatrix} = \sum_{i=1}^{3} e^{\lambda_i t}\mathbf{P}_i \times \begin{pmatrix} N_0^{|0\rangle} \\ N_0^{|\alpha\rangle} \\ N_0^{|\beta\rangle} \end{pmatrix} = \sum_{i=1}^{3} e^{\lambda_i t}\mathbf{P}_i \times \begin{pmatrix} N_{\mathrm{tot}} - N_0^{|\alpha\rangle} \\ N_0^{|\alpha\rangle} \\ 0 \end{pmatrix} \tag{S2}$$

where $\mathbf{P}_i$ is given by the Lagrange-Sylvester formula

$$\mathbf{P}_i = \prod_{\substack{j=1 \\ j\neq i}}^{3} \left\{ \begin{pmatrix} 0 & k_{\mathrm{Cr}}^{\mathrm{CrGdCr}} & k_{\mathrm{Ln}}^{\mathrm{ZnLnZn}} \\ 0 & -\left(k_{\mathrm{Cr}}^{\mathrm{CrGdCr}} + W_{\mathrm{Cr}\to\mathrm{Ln}}\right) & 0 \\ 0 & W_{\mathrm{Cr}\to\mathrm{Ln}} & -k_{\mathrm{Ln}}^{\mathrm{ZnLnZn}} \end{pmatrix} - \lambda_j \begin{pmatrix} 1 & 0 & 0 \\ 0 & 1 & 0 \\ 0 & 0 & 1 \end{pmatrix} \right\} / \prod_{\substack{j=1 \\ j\neq i}}^{3} \left(\lambda_i - \lambda_j\right) \tag{S3}$$

The eigenvalues are determined from the secular determinant

$$\begin{vmatrix} -\lambda & k_{\mathrm{Cr}}^{\mathrm{CrGdCr}} & k_{\mathrm{Ln}}^{\mathrm{ZnLnZn}} \\ 0 & -\left(k_{\mathrm{Cr}}^{\mathrm{CrGdCr}} + W_{\mathrm{Cr}\to\mathrm{Ln}}\right) - \lambda & 0 \\ 0 & W_{\mathrm{Cr}\to\mathrm{Ln}} & -k_{\mathrm{Ln}}^{\mathrm{ZnLnZn}} - \lambda \end{vmatrix} = (-\lambda)\left(\left(k_{\mathrm{Cr}}^{\mathrm{CrGdCr}} + W_{\mathrm{Cr}\to\mathrm{Ln}}\right) + \lambda\right)\left(k_{\mathrm{Ln}}^{\mathrm{ZnLnZn}} + \lambda\right) = 0 \tag{S4}$$

leading to $\lambda_1 = 0$, $\lambda_2 = -\left(k_{\mathrm{Cr}}^{\mathrm{CrGdCr}} + W_{\mathrm{Cr}\to\mathrm{Ln}}\right)$ and $\lambda_3 = -k_{\mathrm{Ln}}^{\mathrm{ZnLnZn}}$

The introduction of these eigenvalues into eq. S3 gives the three projection operators

$$\mathbf{P}_{\lambda_1=0} = \left(k_{\mathrm{Ln}}^{\mathrm{ZnLnZn}}\right)^{-1}\begin{pmatrix} k_{\mathrm{Cr}}^{\mathrm{CrGdCr}} + \\ W_{\mathrm{Cr}\to\mathrm{Ln}} \end{pmatrix}^{-1}\begin{pmatrix} \begin{pmatrix} k_{\mathrm{Cr}}^{\mathrm{CrGdCr}} + \\ W_{\mathrm{Cr}\to\mathrm{Ln}} \end{pmatrix} & k_{\mathrm{Cr}}^{\mathrm{CrGdCr}} & k_{\mathrm{Ln}}^{\mathrm{ZnLnZn}} \\ 0 & 0 & 0 \\ 0 & W_{\mathrm{Cr}\to\mathrm{Ln}} & \begin{pmatrix} -k_{\mathrm{Ln}}^{\mathrm{ZnLnZn}} + k_{\mathrm{Cr}}^{\mathrm{CrGdCr}} \\ +W_{\mathrm{Cr}\to\mathrm{Ln}} \end{pmatrix} \end{pmatrix} \times \begin{pmatrix} k_{\mathrm{Ln}}^{\mathrm{ZnLnZn}} & k_{\mathrm{Cr}}^{\mathrm{CrGdCr}} & k_{\mathrm{Ln}}^{\mathrm{ZnLnZn}} \\ 0 & k_{\mathrm{Ln}}^{\mathrm{ZnLnZn}} - \begin{pmatrix} k_{\mathrm{Cr}}^{\mathrm{CrGdCr}} \\ +W_{\mathrm{Cr}\to\mathrm{Ln}} \end{pmatrix} & 0 \\ 0 & W_{\mathrm{Cr}\to\mathrm{Ln}} & 0 \end{pmatrix}$$

$$\Rightarrow \mathbf{P}_{\lambda_1=0} = \begin{pmatrix} 1 & 1 & 1 \\ 0 & 0 & 0 \\ 0 & 0 & 0 \end{pmatrix} \tag{S5}$$

$$\mathbf{P}_{\lambda_2=-\left(k_{\mathrm{Cr}}^{\mathrm{CrGdCr}}+W_{\mathrm{Cr}\to\mathrm{Ln}}\right)}=\begin{pmatrix}k_{\mathrm{Cr}}^{\mathrm{CrGdCr}}+\\W_{\mathrm{Cr}\to\mathrm{Ln}}-k_{\mathrm{Ln}}^{\mathrm{ZnLnZn}}\end{pmatrix}^{-1}\begin{pmatrix}k_{\mathrm{Cr}}^{\mathrm{CrGdCr}}+\\W_{\mathrm{Cr}\to\mathrm{Ln}}\end{pmatrix}^{-1}\begin{pmatrix}0 & k_{\mathrm{Cr}}^{\mathrm{CrGdCr}} & k_{\mathrm{Ln}}^{\mathrm{ZnLnZn}}\\0 & -\begin{pmatrix}k_{\mathrm{Cr}}^{\mathrm{CrGdCr}}\\+W_{\mathrm{Cr}\to\mathrm{Ln}}\end{pmatrix} & 0\\0 & W_{\mathrm{Cr}\to\mathrm{Ln}} & -k_{\mathrm{Ln}}^{\mathrm{ZnLnZn}}\end{pmatrix}\times\begin{pmatrix}k_{\mathrm{Ln}}^{\mathrm{ZnLnZn}} & k_{\mathrm{Cr}}^{\mathrm{CrGdCr}} & k_{\mathrm{Ln}}^{\mathrm{ZnLnZn}}\\0 & k_{\mathrm{Ln}}^{\mathrm{ZnLnZn}}-\begin{pmatrix}k_{\mathrm{Cr}}^{\mathrm{CrGdCr}}\\+W_{\mathrm{Cr}\to\mathrm{Ln}}\end{pmatrix} & 0\\0 & W_{\mathrm{Cr}\to\mathrm{Ln}} & 0\end{pmatrix}$$

$$\Rightarrow\mathbf{P}_{\lambda_2=-\left(k_{\mathrm{Cr}}^{\mathrm{CrGdCr}}+W_{\mathrm{Cr}\to\mathrm{Ln}}\right)}=\begin{pmatrix}0 & -\dfrac{k_{\mathrm{Ln}}^{\mathrm{ZnLnZn}}-k_{\mathrm{Cr}}^{\mathrm{CrGdCr}}}{k_{\mathrm{Ln}}^{\mathrm{ZnLnZn}}-k_{\mathrm{Cr}}^{\mathrm{CrGdCr}}-W_{\mathrm{Cr}\to\mathrm{Ln}}} & 0\\0 & 1 & 0\\0 & \dfrac{W_{\mathrm{Cr}\to\mathrm{Ln}}}{k_{\mathrm{Ln}}^{\mathrm{ZnLnZn}}-k_{\mathrm{Cr}}^{\mathrm{CrGdCr}}-W_{\mathrm{Cr}\to\mathrm{Ln}}} & 0\end{pmatrix} \tag{S6}$$

$$\mathbf{P}_{\lambda_3=-k_{\mathrm{Ln}}^{\mathrm{ZnLnZn}}}=\begin{pmatrix}k_{\mathrm{Ln}}^{\mathrm{ZnLnZn}}-k_{\mathrm{Cr}}^{\mathrm{CrGdCr}}\\-W_{\mathrm{Cr}\to\mathrm{Ln}}\end{pmatrix}^{-1}\left(k_{\mathrm{Ln}}^{\mathrm{ZnLnZn}}\right)^{-1}\begin{pmatrix}0 & k_{\mathrm{Cr}}^{\mathrm{CrGdCr}} & k_{\mathrm{Ln}}^{\mathrm{ZnLnZn}}\\0 & -\begin{pmatrix}k_{\mathrm{Cr}}^{\mathrm{CrGdCr}}\\+W_{\mathrm{Cr}\to\mathrm{Ln}}\end{pmatrix} & 0\\0 & W_{\mathrm{Cr}\to\mathrm{Ln}} & -k_{\mathrm{Ln}}^{\mathrm{ZnLnZn}}\end{pmatrix}\times\begin{pmatrix}\begin{pmatrix}k_{\mathrm{Cr}}^{\mathrm{CrGdCr}}\\+W_{\mathrm{Cr}\to\mathrm{Ln}}\end{pmatrix} & k_{\mathrm{Cr}}^{\mathrm{CrGdCr}} & k_{\mathrm{Ln}}^{\mathrm{ZnLnZn}}\\0 & 0 & 0\\0 & W_{\mathrm{Cr}\to\mathrm{Ln}} & \begin{pmatrix}-k_{\mathrm{Ln}}^{\mathrm{ZnLnZn}}+k_{\mathrm{Cr}}^{\mathrm{CrGdCr}}\\+W_{\mathrm{Cr}\to\mathrm{Ln}}\end{pmatrix}\end{pmatrix}$$

$$\Rightarrow\mathbf{P}_{\lambda_3=-k_{\mathrm{Ln}}^{\mathrm{ZnLnZn}}}=\begin{pmatrix}0 & \dfrac{W_{\mathrm{Cr}\to\mathrm{Ln}}}{k_{\mathrm{Ln}}^{\mathrm{ZnLnZn}}-k_{\mathrm{Cr}}^{\mathrm{CrGdCr}}-W_{\mathrm{Cr}\to\mathrm{Ln}}} & -1\\0 & 1 & 0\\0 & -\dfrac{W_{\mathrm{Cr}\to\mathrm{Ln}}}{k_{\mathrm{Ln}}^{\mathrm{ZnLnZn}}-k_{\mathrm{Cr}}^{\mathrm{CrGdCr}}-W_{\mathrm{Cr}\to\mathrm{Ln}}} & 1\end{pmatrix} \tag{S7}$$

The final introduction of eqs S5-S7 into eq S2 yields

$$\begin{pmatrix}N_t^{|0\rangle}\\N_t^{|\alpha\rangle}\\N_t^{|\beta\rangle}\end{pmatrix}=\begin{pmatrix}N_{\mathrm{tot}}\\0\\0\end{pmatrix}+N_0^{|\alpha\rangle}e^{-\left(k_{\mathrm{Cr}}^{\mathrm{CrGdCr}}+W_{\mathrm{Cr}\to\mathrm{Ln}}\right)t}\begin{pmatrix}-\dfrac{k_{\mathrm{Ln}}^{\mathrm{ZnLnZn}}-k_{\mathrm{Cr}}^{\mathrm{CrGdCr}}}{k_{\mathrm{Ln}}^{\mathrm{ZnLnZn}}-k_{\mathrm{Cr}}^{\mathrm{CrGdCr}}-W_{\mathrm{Cr}\to\mathrm{Ln}}}\\1\\\dfrac{W_{\mathrm{Cr}\to\mathrm{Ln}}}{k_{\mathrm{Ln}}^{\mathrm{ZnLnZn}}-k_{\mathrm{Cr}}^{\mathrm{CrGdCr}}-W_{\mathrm{Cr}\to\mathrm{Ln}}}\end{pmatrix}+N_0^{|\alpha\rangle}e^{-k_{\mathrm{Ln}}^{\mathrm{ZnLnZn}}t}\begin{pmatrix}\dfrac{W_{\mathrm{Cr}\to\mathrm{Ln}}}{k_{\mathrm{Ln}}^{\mathrm{ZnLnZn}}-k_{\mathrm{Cr}}^{\mathrm{CrGdCr}}-W_{\mathrm{Cr}\to\mathrm{Ln}}}\\0\\-\dfrac{W_{\mathrm{Cr}\to\mathrm{Ln}}}{k_{\mathrm{Ln}}^{\mathrm{ZnLnZn}}-k_{\mathrm{Cr}}^{\mathrm{CrGdCr}}-W_{\mathrm{Cr}\to\mathrm{Ln}}}\end{pmatrix} \tag{S8}$$

The matrix notation is eventually transformed into the common analytical formula

$$N_t^{|0\rangle}=N_{\mathrm{tot}}-\frac{N_0^{|\alpha\rangle}}{\left(k_{\mathrm{Ln}}^{\mathrm{ZnLnZn}}-k_{\mathrm{Cr}}^{\mathrm{CrGdCr}}-W_{\mathrm{Cr}\to\mathrm{Ln}}\right)}\left[\left(k_{\mathrm{Ln}}^{\mathrm{ZnLnZn}}-k_{\mathrm{Cr}}^{\mathrm{CrGdCr}}\right)e^{-\left(k_{\mathrm{Cr}}^{\mathrm{CrGdCr}}+W_{\mathrm{Cr}\to\mathrm{Ln}}\right)t}-W_{\mathrm{Cr}\to\mathrm{Ln}}e^{-k_{\mathrm{Ln}}^{\mathrm{ZnLnZn}}t}\right] \tag{8}$$

$$N_t^{|\alpha\rangle}=N_0^{|\alpha\rangle}e^{-\left(k_{\mathrm{Cr}}^{\mathrm{CrGdCr}}+W_{\mathrm{Cr}\to\mathrm{Ln}}\right)t} \tag{9}$$

$$N_t^{|\beta\rangle}=\frac{W_{\mathrm{Cr}\to\mathrm{Ln}}N_0^{|\alpha\rangle}}{\left(k_{\mathrm{Ln}}^{\mathrm{ZnLnZn}}-k_{\mathrm{Cr}}^{\mathrm{CrGdCr}}-W_{\mathrm{Cr}\to\mathrm{Ln}}\right)}\left[e^{-\left(k_{\mathrm{Cr}}^{\mathrm{CrGdCr}}+W_{\mathrm{Cr}\to\mathrm{Ln}}\right)t}-e^{-k_{\mathrm{Ln}}^{\mathrm{ZnLnZn}}t}\right] \tag{10}$$

Appendix 2. Projection operator solutions for the complete kinetic scheme modeling $[CrLnCr(L2)_3]^{3+}$.

The complete matrix differential equation for relaxation after presaturation is given by

$$\begin{pmatrix} dN_t^{|0\rangle}/dt \\ dN_t^{|\alpha\rangle}/dt \\ dN_t^{|\beta\rangle}/dt \\ dN_t^{|\gamma\rangle}/dt \\ N_t^{|\delta\rangle}/dt \\ dN_t^{|\varepsilon\rangle}/dt \end{pmatrix} = \begin{pmatrix} 0 & k_{Cr}^{CrGdCr} & k_{Ln}^{ZnLnZn} & 0 & 0 & 0 \\ 0 & -\left(k_{Cr}^{CrGdCr}+W_{Cr\rightarrow Ln}\right) & 0 & k_{Ln}^{ZnLnZn} & 2k_{Cr}^{CrGdCr} & 0 \\ 0 & W_{Cr\rightarrow Ln} & -\left(k_{Ln}^{ZnLnZn}\right) & k_{Cr}^{CrGdCr} & 0 & 0 \\ 0 & 0 & 0 & -\left(k_{Cr}^{CrGdCr}+k_{Ln}^{ZnLnZn}\right) & 2W_{Cr\rightarrow Ln} & 2k_{Cr}^{CrGdCr} \\ 0 & 0 & 0 & 0 & -\left(2k_{Cr}^{CrGdCr}+2W_{Cr\rightarrow Yb}\right) & k_{Ln}^{ZnLnZn} \\ 0 & 0 & 0 & 0 & 0 & -\left(2k_{Cr}^{CrGdCr}+k_{Ln}^{ZnLnZn}\right) \end{pmatrix} \times \begin{pmatrix} N_t^{|0\rangle} \\ N_t^{|\alpha\rangle} \\ N_t^{|\beta\rangle} \\ N_t^{|\gamma\rangle} \\ N_t^{|\delta\rangle} \\ N_t^{|\varepsilon\rangle} \end{pmatrix} \quad \text{(S9)}$$

whose solution is

$$\begin{pmatrix} N_t^{|0\rangle} \\ N_t^{|\alpha\rangle} \\ N_t^{|\beta\rangle} \\ N_t^{|\gamma\rangle} \\ N_t^{|\delta\rangle} \\ N_t^{|\varepsilon\rangle} \end{pmatrix} = \exp\left\{ \begin{pmatrix} 0 & k_{Cr}^{CrGdCr} & k_{Ln}^{ZnLnZn} & 0 & 0 & 0 \\ 0 & -\left(k_{Cr}^{CrGdCr}+W_{Cr\rightarrow Ln}\right) & 0 & k_{Ln}^{ZnLnZn} & 2k_{Cr}^{CrGdCr} & 0 \\ 0 & W_{Cr\rightarrow Ln} & -\left(k_{Ln}^{ZnLnZn}\right) & k_{Cr}^{CrGdCr} & 0 & 0 \\ 0 & 0 & 0 & -\left(k_{Cr}^{CrGdCr}+k_{Ln}^{ZnLnZn}\right) & 2W_{Cr\rightarrow Ln} & 2k_{Cr}^{CrGdCr} \\ 0 & 0 & 0 & 0 & -\left(2k_{Cr}^{CrGdCr}+2W_{Cr\rightarrow Yb}\right) & k_{Ln}^{ZnLnZn} \\ 0 & 0 & 0 & 0 & 0 & -\left(2k_{Cr}^{CrGdCr}+k_{Ln}^{ZnLnZn}\right) \end{pmatrix} t \right\} \times \begin{pmatrix} N_0^{|0\rangle} \\ N_0^{|\alpha\rangle} \\ N_0^{|\beta\rangle} \\ N_0^{|\gamma\rangle} \\ N_0^{|\delta\rangle} \\ N_0^{|\varepsilon\rangle} \end{pmatrix} \quad \text{(S10)}$$

Please note that the eigenvalues λ_i (i = 1-6) of the kinetic matrix are simply given by the opposite values of the six diagonal elements, on which the method of projection operator is applied (see appendix 1).

$$\begin{pmatrix} N_t^{|0\rangle} \\ N_t^{|\alpha\rangle} \\ N_t^{|\beta\rangle} \\ N_t^{|\gamma\rangle} \\ N_t^{|\delta\rangle} \\ N_t^{|\varepsilon\rangle} \end{pmatrix} = \begin{pmatrix} N_{\text{tot}} \\ 0 \\ 0 \\ 0 \\ 0 \\ 0 \end{pmatrix} + P_{\lambda_2} \times \begin{pmatrix} N_0^{|0\rangle} \\ N_0^{|\alpha\rangle} \\ N_0^{|\beta\rangle} \\ N_0^{|\gamma\rangle} \\ N_0^{|\delta\rangle} \\ N_0^{|\varepsilon\rangle} \end{pmatrix} e^{-\left(k_{\text{Cr}}^{\text{CrGdCr}} + W_{\text{Cr}\to\text{Ln}}\right)t} + P_{\lambda_3} \times \begin{pmatrix} N_0^{|0\rangle} \\ N_0^{|\alpha\rangle} \\ N_0^{|\beta\rangle} \\ N_0^{|\gamma\rangle} \\ N_0^{|\delta\rangle} \\ N_0^{|\varepsilon\rangle} \end{pmatrix} e^{-\left(k_{\text{Ln}}^{\text{ZnLnZn}}\right)t} + P_{\lambda_4} \times \begin{pmatrix} N_0^{|0\rangle} \\ N_0^{|\alpha\rangle} \\ N_0^{|\beta\rangle} \\ N_0^{|\gamma\rangle} \\ N_0^{|\delta\rangle} \\ N_0^{|\varepsilon\rangle} \end{pmatrix} e^{-\left(k_{\text{Cr}}^{\text{CrGdCr}} + k_{\text{Ln}}^{\text{ZnLnZn}}\right)t}$$

$$+ P_{\lambda_5} \times \begin{pmatrix} N_0^{|0\rangle} \\ N_0^{|\alpha\rangle} \\ N_0^{|\beta\rangle} \\ N_0^{|\gamma\rangle} \\ N_0^{|\delta\rangle} \\ N_0^{|\varepsilon\rangle} \end{pmatrix} e^{-\left(2k_{\text{Cr}}^{\text{CrGdCr}} + 2W_{\text{Cr}\to\text{Yb}}\right)t} + P_{\lambda_6} \times \begin{pmatrix} N_0^{|0\rangle} \\ N_0^{|\alpha\rangle} \\ N_0^{|\beta\rangle} \\ N_0^{|\gamma\rangle} \\ N_0^{|\delta\rangle} \\ N_0^{|\varepsilon\rangle} \end{pmatrix} e^{-\left(2k_{\text{Cr}}^{\text{CrGdCr}} + k_{\text{Ln}}^{\text{ZnLnZn}}\right)t} \qquad \text{(S11)}$$

Numerical calculations of the projection operators are performed for each lanthanide and for each presaturation pumping powers. For Ln = Yb, a presaturation of 0.1 W/mm^2 yields eq. (S12) and Fig. S24, whereas a presaturation of 3 W/mm^2 yields eq. (S13) and Fig. 10.

$$\begin{pmatrix} N_t^{|0\rangle} \\ N_t^{|\alpha\rangle} \\ N_t^{|\beta\rangle} \\ N_t^{|\gamma\rangle} \\ N_t^{|\delta\rangle} \\ N_t^{|\varepsilon\rangle} \end{pmatrix} = \begin{pmatrix} 1 \\ 0 \\ 0 \\ 0 \\ 0 \\ 0 \end{pmatrix} + \begin{pmatrix} -0.105 \\ 0.104 \\ 0.0008 \\ 0 \\ 0 \\ 0 \end{pmatrix} e^{-6.90\text{E}+02t} + \begin{pmatrix} 1.78\text{E}-05 \\ 0 \\ \text{-}1.78\text{E}-05 \\ 0 \\ 0 \\ 0 \end{pmatrix} e^{-3.20\text{E}+04t} + \begin{pmatrix} -2.85\text{E}-08 \\ 6.61\text{E}-08 \\ 2.85\text{E}-08 \\ \text{-}6.61\text{E}-08 \\ 0 \\ 0 \end{pmatrix} e^{-3.24\text{E}+04t} + \begin{pmatrix} 0.0028 \\ -0.00548 \\ -4.388\text{E}-05 \\ 4.34\text{E}-05 \\ 0.0027 \\ 0 \end{pmatrix} e^{-1.38\text{E}+03t}$$

$$+ \begin{pmatrix} -9.09\text{E}-09 \\ 4.319\text{E}-08 \\ 8.75\text{E}-09 \\ -4.20\text{E}-08 \\ -5.05\text{E}-08 \\ 4.97\text{E}-08 \end{pmatrix} e^{-3.29\text{E}+04t} \qquad \text{(S12)}$$

$$\begin{pmatrix} N_t^{|0\rangle} \\ N_t^{|\alpha\rangle} \\ N_t^{|\beta\rangle} \\ N_t^{|\gamma\rangle} \\ N_t^{|\delta\rangle} \\ N_t^{|\varepsilon\rangle} \end{pmatrix} = \begin{pmatrix} 1 \\ 0 \\ 0 \\ 0 \\ 0 \\ 0 \end{pmatrix} + \begin{pmatrix} -1.26 \\ 1.25 \\ 0.001 \\ 0 \\ 0 \\ 0 \end{pmatrix} e^{-6.90\text{E}+02t} + \begin{pmatrix} 0.00025 \\ 0 \\ -0.00025 \\ 0 \\ 0 \\ 0 \end{pmatrix} e^{-3.20\text{E}+04t} + \begin{pmatrix} -2.385\text{E}-05 \\ 5.525\text{E}-05 \\ 2.345\text{E}-05 \\ -5.485\text{E}-05 \\ 0 \\ 0 \end{pmatrix} e^{-3.24\text{E}+04t} \quad \text{(S13)}$$

$$+ \begin{pmatrix} 0.3955 \\ -0.782 \\ -0.006 \\ 0.006 \\ 0.387 \\ 0 \end{pmatrix} e^{-1.38\text{E}+03t} + \begin{pmatrix} -3.78\text{E}-05 \\ 0.00017 \\ 3.64\text{E}-05 \\ -0.00017 \\ -0.00021 \\ 0.00021 \end{pmatrix} e^{-3.29\text{E}+04t}$$

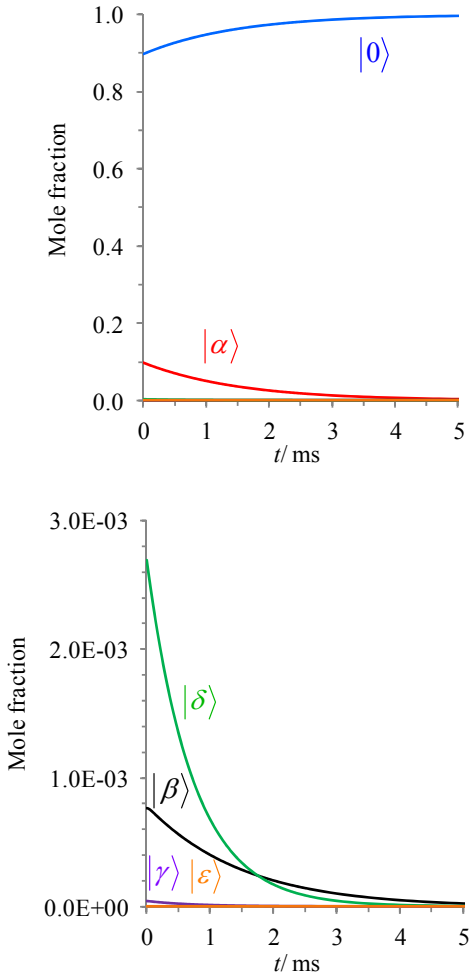

Figure S24 Time evolution of the population densities for the ground state CrYbCr ($|0\rangle$, blue trace) and of the excited states Cr*YbCr ($|\alpha\rangle$, red trace), CrYb*Cr ($|\beta\rangle$, black trace), Cr*Yb*Cr ($|\gamma\rangle$, violet trace), Cr*YbCr* ($|\delta\rangle$, green trace) and Cr*Yb*Cr* ($|\varepsilon\rangle$, orange trace) in $[CrYbCr(\mathbf{L2})_3]^{9+}$ following a 0.1 W/mm^2 presaturation (solid state, 10K, eq. S12).